RICE UNIVERSITY

Influence of Effective Modulus on Period-Doubling Bifurcation in Atomic Force Microscopy: Investigation and Implementation for Sample Characterization

by

Wei Huang

A THESIS SUBMITTED
IN PARTIAL FULFILLMENT OF THE
REQUIREMENTS FOR THE DEGREE

Master of Science

APPROVED, THESIS COMMITTEE

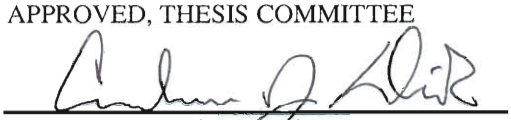

Dr. Andrew J. Dick, Chair
Assistant Professor, Mechanical
Engineering & Materials Science

Dr. Fathi Ghorbel
Professor, Mechanical Engineering &
Materials Science

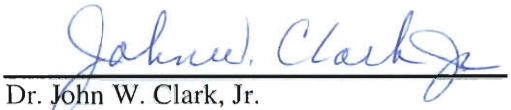

Dr. John W. Clark, Jr.
Professor, Electrical and Computer
Engineering

HOUSTON, TEXAS
November 2010

Abstract

Influence of Effective Modulus on Period-Doubling Bifurcation in Atomic Force Microscopy: Investigation and Implementation for Sample Characterization

by

Wei Huang

Atomic force microscope (AFM) is an important tool for measuring the topographical and other properties of a sample with nanometer resolution. The cantilever probe of the AFM is influenced by nonlinear interaction forces which act between the probe and the sample. For certain non-standard excitation conditions, this can result in bifurcations in the probe's response. This work numerically examines a period-doubling bifurcation observed to occur for interactions with soft materials. The influence of the sample properties and other conditions on the bifurcation is studied and a method is proposed for sample material characterization. The identified values from simulated 1-D and 2-D scans agree well with the true values. The proposed method does not require the use of special probes and it uses the control algorithm for traditional tapping mode AFM with minor modification. This proposed method could also achieve high scan speeds and prevent strong, destructive interaction forces.

Acknowledgments

I want to use this opportunity to thank my advisor, Professor Andrew J. Dick. This thesis could not have been possible without his support. He shows great enthusiasm in the research, and provides me the vital ideas and encouragement during the two and a half years. I also want to thank Professor John W. Clark, Jr. and Professor Fathi H. Ghorbel. It is my honor to have them in my thesis committee. They help me a lot in completing this final version of the thesis.

I own my deepest gratitude to my family. They have sacrificed a lot for my study and they always support me and believe in me.

I am grateful that there are a lot of bright graduate students here at Rice University. The other members in my group, Pooya Ghaderi, Parker Eason, Quan Phan and Daniel Rist, have accompanied me in the lab. We help each other to boost the motivation and relieve the stress. It is also a pleasure to live with other Chinese, American and foreign students and staff at Rice University. The life would not have been so colorful without variety of activities, which they organized.

Finally, I want to show my gratitude to my old friends, both in China and in other countries. They are always willing to share their stories and feelings with me. The sincere friendship is the everlasting source of my courage and happiness.

Contents

Abstract ii

Acknowledgments iii

Chapter 1 Introduction 1

Chapter 2 Background and Literature Review 3

Chapter 3 Materials and Method 11

3.1 Acquisition of Experimental Data 11

3.2 Modeling of AFM 13

3.3 Floquet Theory 23

3.4 Computational Tools 25

Chapter 4 Identification of Nonlinear Relationship and Bifurcation Phenomena 26

4.1 The Bifurcation Process 26

4.2 The Bifurcation Diagram 33

4.3 Floquet Analysis 36

Chapter 5 Parametric Study and the Robustness of the Relations 38

5.1 Varying the Excitation Amplitude 38

5.2 Varying the Quality Factor 40

5.3 Varying the Cantilever Stiffness 41

5.4 Varying the Interaction Model 42

Chapter 6 Fast Scan Scheme 44

6.1 Control Algorithm 44

6.2 1-D Scan 46

6.3 Raster Scan 50

6.4 Summary of the Scan Scheme 54

Chapter 7 Concluding Remarks 56

7.1 Summary 56

7.2 Future Work 57

Reference 58

Chapter 1 Introduction

1.1 Motivation

There are rich nonlinear phenomena in atomic force microscope (AFM) and they are generally avoided and not used in enhancing the capacity of the device. In the dynamic modes of AFM the probe in the device is driven to oscillate. Traditionally the driving frequency is near the fundamental frequency of the cantilever. The bi-stabilities and bifurcation sets are found when the probe tip on the cantilever 'feels' interaction force between it and the sample *e.g.* (Lee, Howell, & Raman, 2003). However, these nonlinear behaviors are not desirable since they cause unstable image conditions and artifacts in the measurement result. The nonlinearities are intrinsic in AFM. They are a popular topic in the area and a lot of work is done to improve the understanding of the nonlinearities. A recent review is available (Stark R. W., 2010).

Though the nanometer resolution of the topographical measurement has been achieved, the AFM has potential to provide more information. This includes quantitative reconstruction of interaction forces in liquid environment and scan on delicate and soft material. These applications are important since the interaction force can be used to identify constitutive properties, chemical properties and the nano-structure of the sample. Many research efforts study intrinsically soft biomaterials.

This work studies the period-doubling bifurcation in atomic force microscope (AFM) numerically and proposes a scan method of measuring the effective modulus of the soft samples based on the bifurcation.

1.2 Thesis Overview

Some of the work in the thesis has been presented in 2009 ASME International Design Engineering Technical Conferences and Computers and Information in Engineering Conference (DETC2009) (Dick & Huang, 2010) and 2010 ASME International Design Engineering Technical Conferences and Computers and Information in Engineering Conference (DETC2010) (Huang & Dick, 2010). A paper based on the work in this thesis is going to be published in the Journal of Computational and Nonlinear Dynamics.

The thesis is organized in the following manner. Chapter 2 provides a background on AFM and explores other methods to characterize materials. The system, modeling and simulation tools are described in Chapter 3. In Chapter 4, the reproduction of experimental data and investigation of the bifurcation relationship is presented. In Chapter 5, the robustness of the relationship is explored through parametric studies with several parameters. The proposed scan process is presented in Chapter 6. The concluding remarks are presented in Chapter 7.

Chapter 2 Background and Literature Review

Atomic Force Microscope (AFM) was introduced in 1986 (Binning, Quate, & Gerber, 1986). It has become an important tool in research at the nanometer scale. Unlike the traditional optical microscope or electron microscopes, the key component in AFM is a cantilever beam-style probe with a sharp tip at the free end, which gives this device superb lateral resolution, quantitative vertical resolution and measurable rich interaction between the tip and the sample. The research on mechanical properties and particularly dynamical behavior of the probe plays a significant role in AFM's development.

Key components of the atomic force microscope system are illustrated in Figure 2-1. The tip at the end of the cantilever is placed close to the sample to allow for interactions

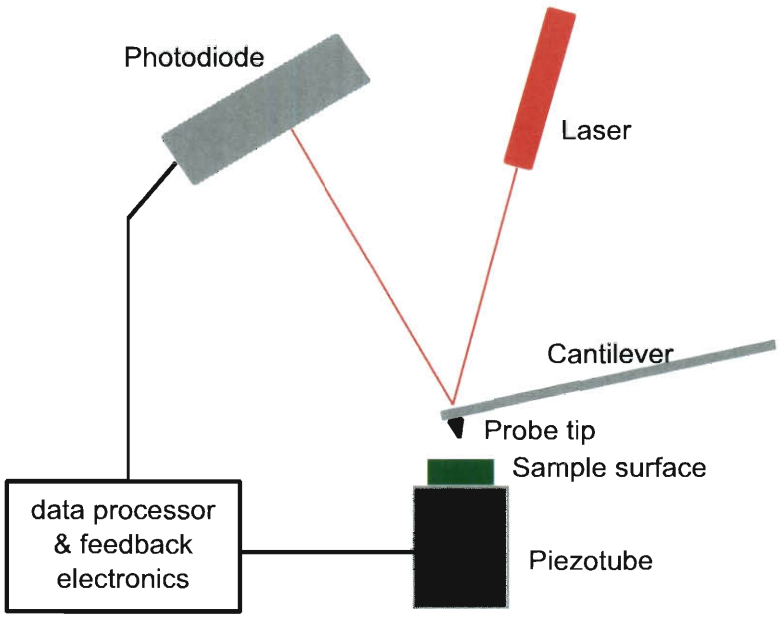

Figure 2-1. Diagram of AFM system

between the atoms at the end of the tip and the atoms of the sample surface. At the same time, the lateral and vertical position of the sample relative to the cantilever is adjustable by feedback controller. This allows the cantilever to "feel" the topography and other properties over an area of the sample. A laser beam is reflected off of the backside of the cantilever near the free end. The deflection of the cantilever changes the slope at the reflection point and the direction of the reflected laser beam. A photodiode element measures the movement of the reflected laser beam. The output of the photodiode is used to calculate the deflection of the probe through a calibration process.

The interaction between the tip and the sample has important influence on the dynamics of the probe and it is a function of the separation distance between the tip and the sample in a nonlinear manner. If the separation distance between the tip and the sample is large, the interaction is negligible. If this distance is small, the interaction is attractive. There is also a repulsive force component if the distance is decreased further and its magnitude increases as the distance continues decreasing. At a certain point the value of the repulsive part is equal to the value of the attractive part and the interaction is neutral. This position is defined as the effective surface of the sample. If the separation distance continuous to decrease, the tip starts to compress the sample and the interaction becomes repulsive. Several models quantify the interaction and can be used in analysis and numerical simulation. Some popular models are the Derjagin-Müller-Toporov (DMT) model (Derjaguin, Muller, & Toporov, 1975), the Johnson-Kendall-Roberts (JRK) model (Johnson, Kendall, & Roberts, 1971) and the Maugis model (Maugis, 1992). The DMT model works well for samples with low adhesion, and the JRK model works well for samples with high adhesion. The Maugis model combines both the conditions with an

adhesion parameter, and is identical to the DMT model or the JRK model at extreme values of the adhesion parameter.

There are several operation modes, including the contact mode, the non-contact mode and the intermittent contact mode (which is also called the tapping mode). The latter two modes are dynamic operation modes. The most important implementations of the non-contact mode and the tapping mode are the frequency modulation mode AFM (FM-AFM) and the amplitude modulation mode AFM (AM-AFM), respectively. Under the contact mode, the tip is placed close to the sample surface to maintain constant influence of repulsive interaction force. The force may change due to the topography in the height of the sample. A feedback loop is used to adjust the position of the probe in order to maintain the level of interaction. The changes in the topography of the sample surface are then directly related to the adjustment in the position of the probe. This constant contact can have multiple drawbacks, such as limitation of scan speed, inelastic deformation of the sample and the wear of the tip. The non-contact mode and the intermittent contact mode can provide improved performance over the contact mode of operation. In FM-AFM and AM-AFM, the cantilever is excited to oscillate and the distance between the tip and the sample surface varies between small or negative values to large values. Only during a small fraction of the operation time is the separation distance small enough to allow significant interaction. In AM-AFM, the interaction force is repulsive at the closest separation distance. In FM-AFM, only attractive interaction forces are experienced. These methods can significantly reduce the extent of contact. Instead of static deflection as in contact mode, the oscillation amplitude is maintained for topographical

measurement in amplitude modulation mode and in frequency modulation mode, the resonance frequency is maintained.

From another point of view, different modes select different quantities as the sources of contrast. The source of contrast must have a strong correlation with the quantity being measured, thus the operation mode monitors the source of contrast in order to measure the desired quantity. For topographical measurement, in which the height of the sample is of interest, the static deflection, the response amplitude and the resonance frequency serve as great sources of contrast in contact mode, amplitude modulation mode and frequency modulation mode, respectively.

In addition to topographical measurement, high resolution mapping of other properties of the sample are of interest and importance to researchers. For example, if the local interaction between the tip and the sample can be measured, the composition and form of the sample may be better understood. Some measurable quantities in the previously mentioned modes are relevant to the interaction, as the phase difference between the driving force and response in amplitude modulation mode and the resonance frequency shift in frequency modulation mode. Some other new methods have been developed and studied. The most common material characterization methods using the atomic force microscope are introduced here.

Frequency-modulation atomic force microscopy is used to measure interaction forces at one point on a sample (Giessibl, 2001). The connection between the resonance frequency and the tip-sample interaction can be elementary and linear if the gradient of the interaction force is constant, as the interaction acts as a linear spring (in the attractive region the spring constant is negative). If the gradient varies during the motion of the

oscillating tip, perturbation method shows the change of the resonance frequency can be approximated as shown in Equation (2.1) which was taken from Giessibl's paper.

$$\Delta f(z_b) = \frac{f_0^2}{kA}\int_0^{1/f_0} F_{ts}(z_b + A\cos(2\pi f_0 t))\cos(2\pi f_0 t)\,dt \qquad (2.1)$$

In the equation, z_b is the vertical base position of the cantilever, f_0 and k are the eigenfrequency and the spring constant of the cantilever, respectively, and F_{ts} is the tip-sample interaction. The approximation is accurate when the energy of the cantilever's oscillations is much larger than the tip-sample potential, which holds well in the operation environment of FM-AFM. In these modes, soft cantilevers are associated with large oscillation amplitude and small oscillation amplitude is associated with very stiff cantilevers, while the interaction is usually in the attractive region, where the force is weak. The frequency shift is measured for a range of separation distance values between the tip and the sample, and then a deconvolution process is used to calculate the interaction force. Experimental results indicate that with a smoothing process, the method can be implemented and give reasonable result which includes the complete attractive region and a portion of the repulsive region. This method requires high-vacuum environment.

Atomic force acoustic microscopy can provide nanometer scale elastic-property mapping (Hurley, Kopycinska-Müller, Kos, & Geiss, 2005). This method operates with repulsive interaction between the probe tip and the sample, and measures the indentation modulus, which is a characteristic of the interaction in the repulsive region. This method also uses the shift of the resonant frequency as the source of contrast. The use of a dynamic implementation allows the method to measure thin films with the thickness

above 50 nm, which is an improvement since the traditional contact nanoindentation method requires thicker samples. Unlike in the FM-AFM, a wide sweep of the excitation frequency at a single point on the sample is necessary to determine the resonance frequency, and this limits the speed of the method. Since the oscillations in this method is purely in the repulsive region and the amplitude is very small, the local indentation modulus instead of a force curve is calculated from the frequency shift. Its lateral resolution is on the order of tens of nanometers, which is good enough to measure the mechanical properties of relatively large nano-scale structures, but is limited in investigating mechanical behavior at smaller scales.

Scanning probe acceleration microscopy (SPAM) is used to measure the tip-sample interaction force simultaneously with topographical information in fluid environments (Legleiter, Park, Cusick, & Kowalewski, 2006). A single degree of freedom, driven, damped oscillator model is used, as shown in Equation (2.2).

$$m_{eff}[\ddot{y} - a_0\omega^2 \sin(\omega t)] + b[\dot{y} + a_0\omega \cos(\omega t)] + ky = F_{ext} \qquad (2.2)$$

In the equation, y is the deflection of the cantilever, m_{eff} is the effective mass of a cantilever, b is the damping coefficient, k is the cantilever spring constant, a_0 is the driving amplitude, ω is the driving frequency, and F_{ext} is the tip-sample force. It should to be noted that the difference between the position of the probe and the deflection of the cantilever is considered in the model. This is necessary since in a fluid environment the excitation amplitude can be on the same scale as the cantilever deflection due to high damping. This is also true for off-resonance excitation. The equation is solved for the second order derivative term (i.e. probe acceleration), as shown in Equation (2.3).

$$\ddot{y} = \frac{1}{m_{eff}}\left[F_{ext} - b\dot{y} - ky + m_{eff}\omega^2 a_0 \sin(\omega t) - b a_0 \omega \cos(\omega t)\right] \quad (2.3)$$

The method uses the pulse-like component of the second order derivative of the cantilever deflection as the source of contrast for the interaction force, utilizing the fact that the changing rate for the interaction force is much faster than the other terms in the right hand side of Equation (2.3). The configuration and control method in its operation are based on tapping-mode AFM, and the significant influence between the probe and the sample is very short in time. The higher harmonic components in the response are strengthened in the liquid environment, which makes the denoise filter more efficient. Meanwhile, the filter is necessary since the liquid environment also causes a low signal to noise level. Since the second order numerical derivative is used, the result is still not smooth. This method does not measure a force curve but is most interested in the maximum interaction force. Legleiter *et al.* demonstrated a scan rate of 5 Hz corresponding to a 2.5-μm line. The problem is that the high level of the higher harmonic components may require the use of a multiple mode modeling method. The limitations from the noisy liquid environment and the signal lost through a strong filter reduce the sensitivity considerably and limit the ability of quantitative measurement for this method. It should be noted that these limitations affect other methods in liquid environments, as well.

A specially designed torsional harmonic cantilever can be used to map the interaction force curve while obtaining topographical information through a scan process (Sahin, Magonov, Su, Quate, & Solgaard, 2007). The tip is not placed on the long axis of the cantilever. Instead, an offset is added. The tip-sample interaction then will excite both flexural modes and torsional modes. The flexural oscillations are still used to collect

topographic information. The torsional mode is used to calculate the tip-sample interaction force by using the transfer function approach (Stark, Guckenberger, Stemmer, & Stark, 2005). The input includes the excitation and the tip-sample interaction. The output is the photodiode readout. The transfer function between the readout and the interaction is modeled and calibrated prior to the scan. Then it is used to calculate the interaction from the actual measurement. The torsional mode is superior to the flexural mode because a higher signal-to-noise ratio can be achieved. The coexistence of two modes helps in collecting more information.

This thesis examines the period-doubling bifurcation in the tapping-mode AFM and discovered its potential as a new source of contrast for the measurement of the effective modulus of the interaction. The effective modulus is a localized property which depends on the Young's modulus and Poisson's ratio of the tip and the sample. The relation between the characteristics of the bifurcation and the effective modulus is modeled. A measurement scheme based on the relation is proposed and numerically studied.

Chapter 3 Materials and Method

This thesis studies the period-doubling bifurcation, which is inspired by some experimental work. Here the previous experimental observation is introduced. The model and simulation tools are also introduced.

3.1 Acquisition of Experimental Data

Professor Dick and his co-researchers in Japan collected the experimental data with a commercial atomic force microscope (Dick, et al., 2009). The cantilever in the AFM is made of silicon and the shape of the cross-sections for most of its length is uniform rectangular. There is a probe tip at the free end of the cantilever and its mass is considered in the model. The image of the cantilever is shown in Figure 3-1.

The sample is one layer of silicone rubber mounted on the glass substrate. The operation frequency of the AFM is set to be 2.5 times the probe's fundamental frequency.

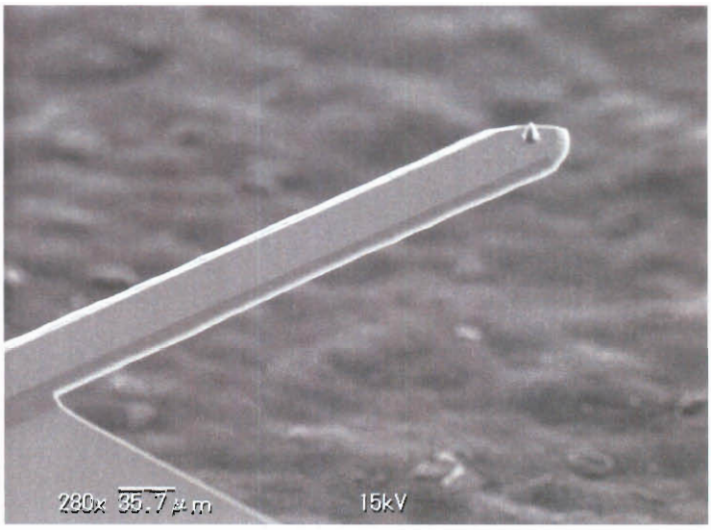

Figure 3-1. The image of the cantilever.

Supplemental data acquisition devices are added to record the voltage of the photodiode sensors. From the voltage, the position of the tip was calculated. Then the data went through a denoise process, which includes applying fast Fourier transform (FFT) on the data, retaining only significant frequency components and applying an inverse FFT. The separation distance between the rest position of probe and the sample is set to decrease in the experiment and the responses of the probe at four different separation distances are illustrated in Figure 3-2.

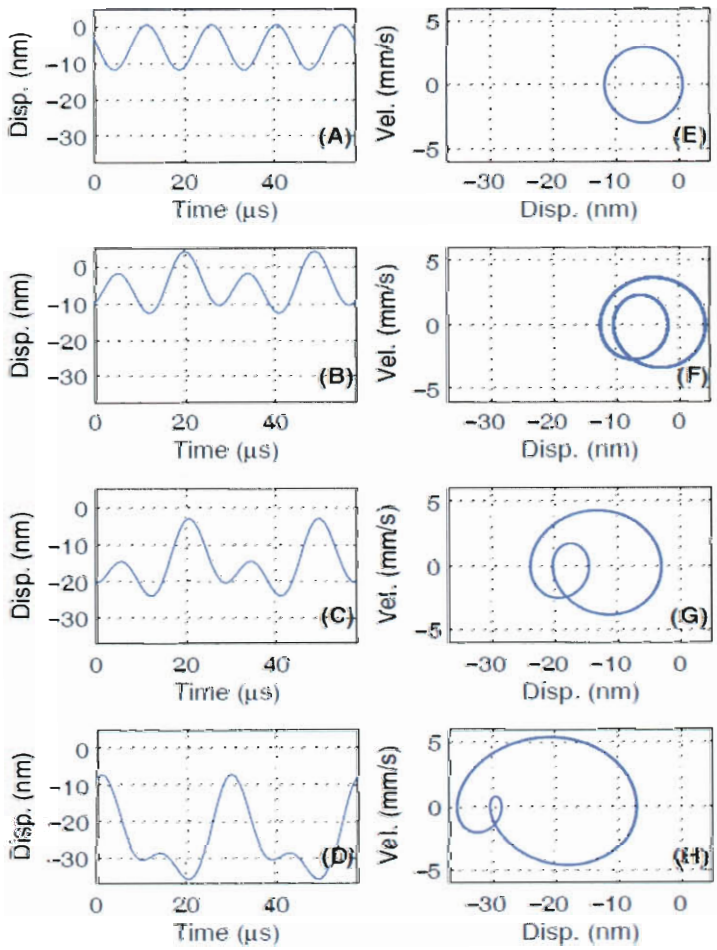

Figure 3-2. Time series plots (A) – (D) and corresponding phase portrait plots (E) – (H) depicting experimental response transition for AFM cantilever probe.

In the set of data, the ordinary sinusoid response undergoes a qualitative change as the cantilever compresses the sample to a greater extent. The most significant characteristic of this process is that the two neighboring local maxima in the response differ in value and the period of the response doubles. In the field of nonlinear dynamics, this is identified as a period-doubling bifurcation. Initial simulations are performed following the experimental procedure to confirm the period-doubling bifurcation. The transition from the physical model to the simulation model involves proper determination of the equations of motion and parameter values.

3.2 Modeling of AFM

Since the parametric study is conducted in this work, several sets of values of the parameters are used. In the description of the modeling, unless otherwise stated, the values are corresponding to the simulation which would confirm the experimental observation.

Not all the specifications of the cantilever used in the experiment are available. In the modeling, the specifications for another cantilever are used and the values are listed in Table 3-1. This cantilever has a similar stiffness and is also suitable for the measurement of soft material.

In the experimental data the free off-resonance oscillation amplitude is around $7\ nm$. Thus the ratio between the oscillation amplitude and the length of the cantilever is about 1.56×10^{-5}. The linear Euler-Bernoulli beam equation is used to represent the system. The dimensional form is shown in Equation (3.1).

$$\hat{E}\hat{I}\frac{\partial^4}{\partial \hat{s}^4}\widehat{W}(\hat{s},\hat{t}) + \hat{\rho}\hat{A}\frac{\partial^2}{\partial \hat{t}^2}\widehat{W}(\hat{s},\hat{t}) = 0 \tag{3.1}$$

In the equation, $\widehat{W}$ is the total displacement of the cantilever, and it is dependent on the coordinate along the cantilever $\hat{s}$ and the time $\hat{t}$. The values of the cantilever parameters $\hat{E}$, $\hat{I}$, $\hat{\rho}$ and $\hat{A}$ can be obtained from Table 3-1.

Table 3-1. List of Dimensional Parameters for the cantilever.

Parameter	Symbol (Units)	Value
Cantilever Young's modulus	$\hat{E}\ (GPa)$	118.92
Cantilever material density	$\hat{\rho}\ (kg/m^3)$	2.1539×10^3
Cantilever length	$\hat{L}\ (m)$	4.50×10^{-4}
Cantilever width	$\hat{b}\ (m)$	4.00×10^{-5}
Cantilever thickness	$\hat{h}\ (m)$	5.00×10^{-6}
Force constant	$\hat{k}\ (N/m)$	2
Cantilever fundamental resonance frequency	$\widehat{\omega_0}\ (kHz)$	28
Ratio of probe tip mass to cantilever mass	γ	0.03

In this work, the moving base of the cantilever is modeled as a moving reference frame. In order to derive the equation in the moving frame, the total beam displacement is defined in Equation (3.2).

$$\widehat{W}(\hat{s},\hat{t}) = \widehat{w}(\hat{s},\hat{t}) + \hat{X}(\hat{t}) \tag{3.2}$$

In the equation, $\widehat{w}$ the relative deflection of the cantilever, and $\hat{X}$ is the displacement of the base of the cantilever.

In this configuration, the base excitation produces an inertial force and the relative deflection of the cantilever is separated from the base motion. The base motion is the input and a known term as $\hat{X}(\hat{t}) = \widehat{X_0}\cos(2.5\ \widehat{\omega_0}\ \hat{t})$, where $\widehat{X_0}$ is the excitation amplitude.

The deflection is also the measured quantity. The new equation is shown in Equation (3.3).

$$\hat{E}\hat{I}\frac{\partial^4}{\partial \hat{s}^4}\hat{w}(\hat{s},\hat{t}) + \hat{\rho}\hat{A}\frac{\partial^2}{\partial \hat{t}^2}\hat{w}(\hat{s},\hat{t}) = -\hat{\rho}\hat{A}\frac{d^2}{d\hat{t}^2}\hat{X}(\hat{t}) \tag{3.3}$$

Its dimensionless form is shown in Equation (3.4). The relations between the dimensional terms and dimensionless terms are shown in Equation (3.5) through Equation (3.8).

$$\frac{\partial^4}{\partial s^4}w(s,t) + \frac{\partial^2}{\partial t^2}w(s,t) = -\frac{d^2}{dt^2}X(t) \tag{3.4}$$

$$\hat{W} = w\,\hat{L} \tag{3.5}$$

$$\hat{s} = s\,\hat{L} \tag{3.6}$$

$$\hat{X} = X\,\hat{L} \tag{3.7}$$

$$\hat{t} = t\sqrt{\frac{\hat{\rho}\hat{A}}{\hat{E}\hat{I}}}\,\hat{L}^2 \tag{3.8}$$

In the equations, $\hat{L}$ is the length of the cantilever and the symbols without the "hat" (^) are the dimensionless forms of corresponding parameters. The cantilever is part of a much bigger material which is used to mount the probe in the AFM. In the moving frame, the deflection and slope at the excitation end are assumed to be zero. At the other end with the tip, the moment is zero and the shear force is equal to the sum of the tip-sample interaction force and the inertial force due to the moving frame and the tip mass. Finally, the boundary conditions for the equation are shown in Equation (3.9) through (3.12).

$$w(s,t)|_{s=0} = 0 \tag{3.9}$$

$$\frac{\partial}{\partial s}w(s,t)\Big|_{s=0} = 0 \tag{3.10}$$

$$\left.\frac{\partial^2}{\partial s^2} w(s,t)\right|_{s=1} = 0 \tag{3.11}$$

$$\left.\frac{\partial^3}{\partial s^3} w(s,t)\right|_{s=1} = \gamma\left[\left.\frac{\partial^2}{\partial t^2} w(s,t)\right|_{s=1} + \frac{d^2}{dt^2} X(t)\right] + F_{ts}\big(w(1,t)\big) \tag{3.12}$$

In Equation (3.12), γ is the ratio between the probe tip mass and the cantilever mass, $w(1,t)$ is the dimensionless deflection of the free end of the cantilever probe, and F_{ts} is the dimensionless interaction force between the probe tip and the sample. The relation between the dimensional force term and the dimensionless force term is defined in Equation (3.13).

$$\widehat{F_{ts}} = F_{ts}\frac{\hat{E}\hat{I}}{\hat{L}^2} \tag{3.13}$$

Two different interaction force models are used in this work. The DMT model has the form in Equation (3.14) and Equation (3.15).

$$\widehat{F_{ts}}\big(\widehat{w_{tip}}\big) = \begin{cases} -\dfrac{\hat{H}\hat{R}}{6\hat{\sigma}^2} & \hat{\sigma} < -\hat{d} \\ -\dfrac{\hat{H}\hat{R}}{6\hat{d}^2} + \dfrac{4}{3}\widehat{E^*}\sqrt{\hat{R}}\big(\hat{\sigma}+\hat{d}\big)^{3/2} & \hat{\sigma} \geq -\hat{d} \end{cases} \tag{3.14}$$

$$\hat{\sigma} = \widehat{w_{tip}} + \hat{X}(\hat{t}) - \hat{\delta}(\hat{t}) + \left(\frac{\hat{H}\sqrt{\hat{R}}}{8\widehat{E^*}\hat{d}^2}\right)^{\frac{2}{3}} - \hat{d} \tag{3.15}$$

In the equations, $\widehat{w_{tip}} = \widehat{w}(1,\hat{t})$, which is the deflection of the probe tip, $\hat{\delta}$ is the vertical distance between the rest position of the cantilever base and the sample which is defined as the nominal separation distance in the rest of the thesis, $\hat{H}$ is the Hamaker constant, $\hat{R}$ is the AFM probe tip radius, $\hat{d}$ is the interatomic spacing and $\widehat{E^*}$ is the effective modulus of the interaction between the probe tip and the sample. The form of Equation (3.15) is

chosen in order to satisfy that the interaction force is zero at the effective surface, where the distance between the tip and the sample $\hat{\delta}(\hat{t}) - \left(\widehat{w_{tip}} + \hat{X}(\hat{t})\right)$ is equal to zero. The effective modulus of the interaction $\widehat{E^*}$ is given in Equation (3.16).

$$\frac{1}{\widehat{E^*}} = \frac{1-\widehat{\upsilon_t}^2}{\widehat{E_t}} + \frac{1-\widehat{\upsilon_s}^2}{\widehat{E_s}} \tag{3.16}$$

In the equations, $\widehat{\upsilon_t}$, $\widehat{E_t}$, $\widehat{\upsilon_s}$ and $\widehat{E_s}$ are the Poisson's ratio and Young's modulus of the tip and the sample, respectively.

The values of the parameters in the DMT model are listed in Table 3-2. They correspond to the interaction between a silicon probe tip and silicone rubber sample and the interaction between a silicon probe tip and glass sample, respectively.

Table 3-2. Dimensional Parameter values for DMT atomic interaction force model

Parameter (Units)	Silicone Rubber Sample	Glass Sample
$\hat{H}\ (Nm)$	4.5×10^{-20}	6.6×10^{-20}
$\hat{R}\ (m)$	10×10^{-9}	10×10^{-9}
$\hat{d}\ (m)$	0.165×10^{-9}	0.170×10^{-9}
$\widehat{E^*}\ (GPa)$	4.50×10^{-3}	$3.00 \times 10^{+1}$

The curves of the interaction force values versus the separation distances between the probe tip and the sample are illustrated in Figure 3-3.

The slope of the force curve at the effective surface of the sample is defined as the effective stiffness of the sample. When the two sample materials are compared, large differences between the values of the effective modulus $\widehat{E^*}$ in Table 3-2 and the values of

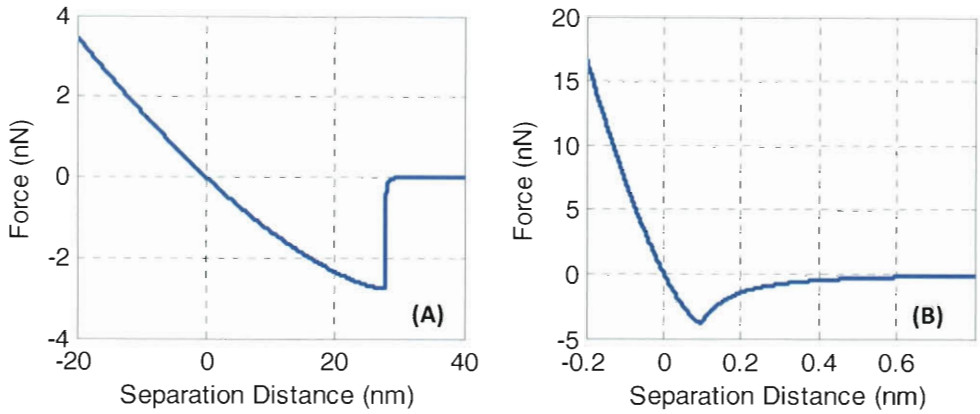

Figure 3-3. Force value-versus-separation distance curves for (A) silicone rubber sample, (B) glass sample.

the effective stiffness in Figure 3-3 are noticed. Since the sample in the previously mentioned experiment consists of a layer of silicone rubber on glass substrate, the effective modulus is believed to be between $4.50 \times 10^{-3}\ GPa$ and $30\ GPa$. In the simulation, which is firstly aimed at numerically reproducing the experimental observation, the effective modulus $\widehat{E^*}$ is tuned, while the values of the other parameters corresponding to the silicone rubber sample are used.

Another interaction force model is used in the work for the purpose of the parametric study. This model is identified as the empirical model in this thesis. It is used to fit the force-versus-distance data from molecular dynamic (Solares & Crone, 2007). The empirical interaction force model has the form in Equation (3.17) and Equation (3.18).

$$\widehat{F_{ts}}\left(\widehat{w_{tip}}\right) = \begin{cases} -\dfrac{\widehat{W}}{1 + \hat{A}\hat{\sigma}^2} & \hat{\sigma} < 0 \\ \hat{S}\hat{\sigma}^2 - \widehat{W} & \hat{\sigma} \geq 0 \end{cases} \tag{3.17}$$

$$\hat{\sigma} = \widehat{w_{tip}} + \hat{X}\,(\hat{t}) - \hat{\delta}(\hat{t}) + \sqrt{\frac{\widehat{W}}{\hat{S}}} \tag{3.18}$$

In the equations, $\widehat{W}$, $\hat{S}$, and $\hat{A}$ are parameters associated with the empirical model. Similar to Equation (3.15), the form of Equation (3.18) is chosen in order to satisfy the zero interaction condition at the effective surface. It should be noted that this empirical model and the DMT model have different hardening behaviors while both of them consist the attractive part and the repulsive part and are defined in a piece-wisely fashion. In this work, the values of the parameters in the empirical model are calculated from the ones in the DMT model by using Equation (3.19) and Equation (3.20).

$$\widehat{W} = \frac{\widehat{H}\widehat{R}}{6\,\hat{d}^2} \tag{3.19}$$

$$\hat{S} = \frac{3}{2}\left(\frac{\hat{d}^2\widehat{E^*}^4\hat{R}}{\widehat{H}}\right)^{\frac{1}{3}} \tag{3.20}$$

These equations are calculated to match the effective stiffness and the maximum attractive force of the empirical model to the corresponding values of the DMT model. The value of the other parameter $\hat{A}$ is manually selected to match the shape of the interaction force curve in the attractive region, and is set to a fixed value $1 \times 10^{20}\ m^{-2}$.

In order to solve Equation (3.4) numerically, a multimode approximation and the Galerkin method are used. The Galerkin method is used with a multimode approximation in order to discretize the partial differential equation into several ordinary differential equations. It is assumed that the response is the superposition of the products of its normal modes and corresponding general modal coordinates. If the excitation frequency is close to one of the eigenfrequency, only that corresponding mode is significant. In this work, the off-resonance excitation requires the use of multiple modes. Previous work has shown that three modes are sufficient for the off-resonance condition near two-and-a-half

times the fundamental frequency (Dick, et al., 2009). Thus the dimensionless deflection of the cantilever is expressed as Eqn. (3.21).

$$w(s,t) = \sum_{m=1}^{3} \phi_m(s) q_m(t) \tag{3.21}$$

The functions $q_n(t)$ are general modal coordinates. The functions $\phi_n(s)$ are mode shapes. In order to calculate the mode shapes, the conservative and un-excited forms of Equation (3.4) and Equation (3.9) through Equation (3.12), as shown in Equation (3.22) through Equation (3.26), are used

$$\frac{\partial^4}{\partial s^4} w(s,t) + \frac{\partial^2}{\partial t^2} w(s,t) = 0 \tag{3.22}$$

$$w(s,t)|_{s=0} = 0 \tag{3.23}$$

$$\frac{\partial}{\partial s} w(s,t)\Big|_{s=0} = 0 \tag{3.24}$$

$$\frac{\partial^2}{\partial s^2} w(s,t)\Big|_{s=1} = 0 \tag{3.25}$$

$$\frac{\partial^3}{\partial s^3} w(s,t)\Big|_{s=1} = \gamma \frac{\partial^2}{\partial t^2} w(s,t)\Big|_{s=1} \tag{3.26}$$

The solution is assumed to be periodic in the form shown in Equation (3.27).

$$w(s,t) = \phi(s) e^{i\omega t} \tag{3.27}$$

In the equation, $\phi(s)$ is the mode shape function and ω is the eigenfrequency. Equation (3.27) is substituted into Equation (3.22) through Equation (3.26). The equations for the mode shape function are shown in Equation (3.28) through Equation (3.32).

$$\phi''''(s) - \beta^2\phi(s) = 0 \tag{3.28}$$

$$\phi(0) = 0 \tag{3.29}$$

$$\phi'(0) = 0 \tag{3.30}$$

$$\phi''(1) = 0 \tag{3.31}$$

$$\phi'''(1) + \gamma\beta^4\phi(1) = 0 \tag{3.32}$$

In these equations, $\beta^2 = \omega$. The form of the solution to Equation (3.28) through Equation (3.30) is given by Equation (3.33).

$$\phi(s) = C_1(\sin(\beta s) - \sinh(\beta s)) + C_2(\cos(\beta s) - \cosh(\beta s)) \tag{3.33}$$

In this equation, C_1 and C_2 are constants. When Equation (3.33) is substituted into Equation (3.31) and Equation (3.32), the equation to determine β, C_1 and C_2, is obtained, as shown in Equation (3.34) .

$$\begin{bmatrix} -\beta^2\sin(\beta) - \beta^2\sinh(\beta) & -\beta^2\cos(\beta) - \beta^2\cosh(\beta) \\ \begin{pmatrix} -\beta^3\cos(\beta) - \beta^3\cosh(\beta) \\ +\beta^4\gamma\sin(\beta) - \beta^4\gamma\sin(\beta) \end{pmatrix} & \begin{pmatrix} \beta^4\gamma\cos(\beta) - \beta^4\gamma\cosh(\beta) \\ +\beta^3\sin(\beta) - \beta^3\sinh(\beta) \end{pmatrix} \end{bmatrix} \begin{bmatrix} C_1 \\ C_2 \end{bmatrix} = 0 \tag{3.34}$$

The determinant of the coefficient matrix needs to be zero for the existence of non-zero values of C_1 and C_2. The three smallest roots are listed as β_1, β_2 and β_3. They give the three eigenfrequencies ω_1, ω_2 and ω_3. The values of C_1 and C_2 are calculated for each value of β, and their values are scaled to satisfy the normalization condition shown in Equation (3.35).

$$\gamma\phi_n^2(1) + \int_0^1 \phi_n^2(s)\, ds = 1 \qquad n = 1,2,3 \tag{3.35}$$

Since a finite number of modes are used, Equation (3.4) may no longer hold. The error or residual is shown in Equation (3.36).

$$\epsilon = \frac{\partial^4}{\partial s^4} w(s,t) + \frac{\partial^2}{\partial t^2} w(s,t) + \frac{d^2}{dt^2} X(t) \tag{3.36}$$

In the Galerkin method, the approximation in Equation (3.21) is used, the product of the residual and the shape function is integrated over the length of the cantilever, and the weighted integral is set to zero. This is shown in Equation (3.37).

$$\int_0^1 \left(\frac{\partial^4}{\partial s^4} \left(\sum_{m=1}^{3} \phi_m(s) q_m(t) \right) + \frac{\partial^2}{\partial t^2} \left(\sum_{m=1}^{3} \phi_m(s) q_m(t) \right) + \frac{d^2}{dt^2} X(t) \right) \phi_n(s)\, ds = 0 \quad n = 1,2,3 \tag{3.37}$$

Integration by parts and the boundary conditions in Equation (3.9) through Equation (3.12) are used to derive the ordinary differential equations for the general modal coordinates. As a result of the normalization of the modes shapes, the resulting equations are of the form presented in Equation (3.38).

$$\frac{d^2}{dt^2} q_n(t) + \frac{\omega_n}{Q_n} \frac{d}{dt} q_n(t) + \omega_n^2 q_n(t) = f_{b,n}(t) + f_{ts,n}(w_{tip}) \quad n = 1,2,3 \tag{3.38}$$

Several things should be noted. Due to the orthogonality of the mode shapes, the left parts of the equations are uncoupled. However, the three modal responses are still coupled by the tip-sample interaction force term, which depends on the total probe deflection and thus every modal response. The interaction force and inertial force are

transferred from the boundary conditions into the ordinary differential equations. The modal forces are defined in Equation (3.39) and Equation (3.40)(3.40), respectively.

$$f_{b,n}(t) = -\int_0^1 \phi_n(s)\, ds \frac{d^2}{dt^2} X(t) \tag{3.39}$$

$$f_{ts,n}(w_{tip}) = -\phi_n(1) F_{ts}(w_{tip}) \tag{3.40}$$

A viscous damping term is also added to account for the energy dissipation, and Q_n are the quality factors. The values of Q_n are set to 10 in the simulation. The damping level corresponding to this value is higher than the normal damping level in the air environment, and the reasons will be explained later in the parametric study.

3.3 Floquet Theory

Within this work, a bifurcation in dynamic response of an AFM is studied. The bifurcation results in a change in the stability of the existing periodic solutions and the creation of a new solution. Floquet theory is an important tool used to study the stability of periodic solutions (Nayfeh & Balachandran, 1995).

Here the summary of the procedure for applying Floquet theory is presented. In the pursuit of simplicity, the state space form of the equation is used without the explicitly expressed dependence on all variables. The system is shown as Equation (3.41).

$$\dot{x(t)} = F(x(t), t; M) \tag{3.41}$$

In the equation, $x(t) = [q_1(t)\ q_2(t)\ q_3(t)\ \dot{q}_1(t)\ \dot{q}_2(t)\ \dot{q}_3(t)]^T$ is the six-dimensional state vector for the model used in this study and M is the parameter vector, which includes the parameters for the cantilever, the excitation and the tip-sample interaction.

In order to study the stability of a periodic solution of this system, $x(t)$ is assumed to have the form in Equation (3.42)

$$x(t) = X_0(t) + z(t) \tag{3.42}$$

In the equation, $X_0(t)$ is a known periodic solution to Equation (3.41) and $z(t)$is a small disturbance. Equation (3.41) is expanded into a Taylor series and only linear term of $z(t)$ is kept based upon the assumption of small disturbances. This yields Equation (3.43).

$$\dot{z}(t) = D_x F(X_0, t; M_0)\, z(t) + O(\|z(t)\|^2) \quad \text{or} \quad \dot{z}(t) = A(t, M_0) z(t) \tag{3.43}$$

In this equation, $A(t, M_0) = D_x F(X_0, t; M_0)$ is the matrix of first partial derivatives of F with respect to the state variables. It is evaluated with the periodic solution X_0. The matrix is shown in Equation (3.44).

$$D_x F(X_0, t; M_0) = \begin{bmatrix} 0 & 0 & 0 & 1 & 0 & 0 \\ 0 & 0 & 0 & 0 & 1 & 0 \\ 0 & 0 & 0 & 0 & 0 & 1 \\ \frac{\partial f_{ts,1}(w_{tip})}{\partial w_{tip}}\phi_1(1) - \omega_1^2 & \frac{\partial f_{ts,1}(w_{tip})}{\partial w_{tip}}\phi_2(1) & \frac{\partial f_{ts,1}(w_{tip})}{\partial w_{tip}}\phi_3(1) & -\frac{\omega_1}{Q_1} & 0 & 0 \\ \frac{\partial f_{ts,2}(w_{tip})}{\partial w_{tip}}\phi_1(1) & \frac{\partial f_{ts,2}(w_{tip})}{\partial w_{tip}}\phi_2(1) - \omega_2^2 & \frac{\partial f_{ts,2}(w_{tip})}{\partial w_{tip}}\phi_3(1) & 0 & -\frac{\omega_2}{Q_2} & 0 \\ \frac{\partial f_{ts,3}(w_{tip})}{\partial w_{tip}}\phi_1(1) & \frac{\partial f_{ts,3}(w_{tip})}{\partial w_{tip}}\phi_2(1) & \frac{\partial f_{ts,3}(w_{tip})}{\partial w_{tip}}\phi_3(1) - \omega_3^2 & 0 & 0 & -\frac{\omega_3}{Q_3} \end{bmatrix} \tag{3.44}$$

Six solutions of Equation (3.43) form a matrix solution as shown in Equation (3.45).

$$Z(t) = [z_1(t)\ z_2(t)\ z_3(t)\ z_4(t)\ z_5(t)\ z_6(t)] \tag{3.45}$$

Every column of $Z(t)$ is a six-dimensional vector corresponding to one solution. If $Z(0) = \mathbf{I}$, where **I** is a 6×6 identity matrix, after the integration over one period, $Z(T)$ satisfies $Z(T) = Z(0)\, Z(T)$. This results in the monodromy matrix being defined by

$\Phi = Z(T)$. The eigenvalues of the monodromy matrix are known as the Floquet multipliers. The values of the Floquet multipliers offer a method to verify the stability of the periodic solution. The values can be complex numbers. If the norm of none of the values is equal to one (none of the Floquet multipliers lies on the unit circle on the complex plane), the periodic solution is called hyperbolic. The periodic solution is asymptotically stable if all of the Floquet multipliers are inside the unit circle. If at least one of the Floquet multipliers is outside the unit circle, the periodic solution is unstable. If at least one of the Floquet multipliers is on the unit circle for a nonautonomous system, the periodic solution is called non-hyperbolic and a nonlinear analysis is required to verify its stability.

Particularly, during the change of the values of several parameters of the system, if Floquet multipliers leave the unit circle, a bifurcation has occurred. The manner by which they leave the unit circle indicates what type of bifurcation has occurred.

3.4 Computational Tools

Mathematica is used to derive the model. Matlab and AUTO (Doedel, 1981) are used to perform the simulations, including the modeling, numerical integration and post-analysis. Matlab is used to begin the research, simulate and analyze the nominal case, and conduct the scan simulation. AUTO is able to perform a bifurcation analysis quickly and is used for the parametric study.

Chapter 4 Identification of Nonlinear Relationship and Bifurcation Phenomena

The procedure to reproduce the experimental observation is described in this section. After the model is verified, it is used to generate more data in order to build bifurcation diagrams, which is an essential tool in studying the nonlinear behavior. A stability analysis is used to prove that the bifurcation is a period-doubling bifurcation.

4.1 The Bifurcation Process

The frequency of the excitation is 2.5 times the fundamental frequency of the cantilever. The excitation amplitude is tuned in order to match the free off-resonance oscillation amplitude to the value of 7 nm from the experiment, resulting $\widehat{X_0} = 7.55\ nm$.

During the writing of the thesis, one fact is noted that the laser system measures the deflection of the cantilever in the experiment rather than the total displacement. In the finished work the experimental values are matched as the total displacement. In the off-resonance case, the deflection and the base displacement are in the same scale, and re-calibration shows the value of $\widehat{X_0}$ should be $3.63\ nm$. However, the parametric study shows that the behavior is insensitive to small changes of the excitation amplitude and it is believed that this discrepancy does not affect the discussions and conclusions regarding to the period-doubling bifurcation.

The effective modulus in the DMT model is tuned in the simulation. This is done because in the experiment, the accurate value of the separation distance between the probe tip and the sample surface, which is related to the compression, is unknown. The value of the

effective modulus for the interaction between the silicon tip and silicone rubber material is only valid for small compressions. If the compression is large, the contact area will increase, and the thickness of the layer between the tip and the much stiffer glass substrate is decreased. Both factors will increase the effective stiffness of the silicone rubber material. In the simulation, it is discovered that the value of the effective modulus corresponding to the interaction between the silicon tip and the silicone rubber material is too small, and the period-doubling bifurcation is not observed in a reasonable range of compression. It is also discovered that the value of the effective modulus corresponding to the interaction between the silicon tip and the glass material is too large, and a discontinuous secondary Hopf bifurcation is observed. The effective modulus values in a middle range can be used to reproduce the experimental observation. The value $\widehat{E^*} = 0.08518\ GPa$ is used to simulate these conditions.

The simulation is started with the probe far away from the sample and responding to the harmonic excitation. When the distance between the probe and the sample is sufficiently large, the tip-sample interaction is negligible and the base movement is the only source of excitation. The responses of the three modes are simulated and added together, as shown in Figure 4-1.

As shown in these figures, the frequency of the response is the same as the frequency of the excitation. Under off-resonance excitation, the response of first mode is still the most significant component. The amplitudes of the oscillation corresponding to the second and third mode shapes are 8.7% and 0.55% of the amplitude corresponding to the first mode shape, respectively. Because of the phase difference between the relative deflection and

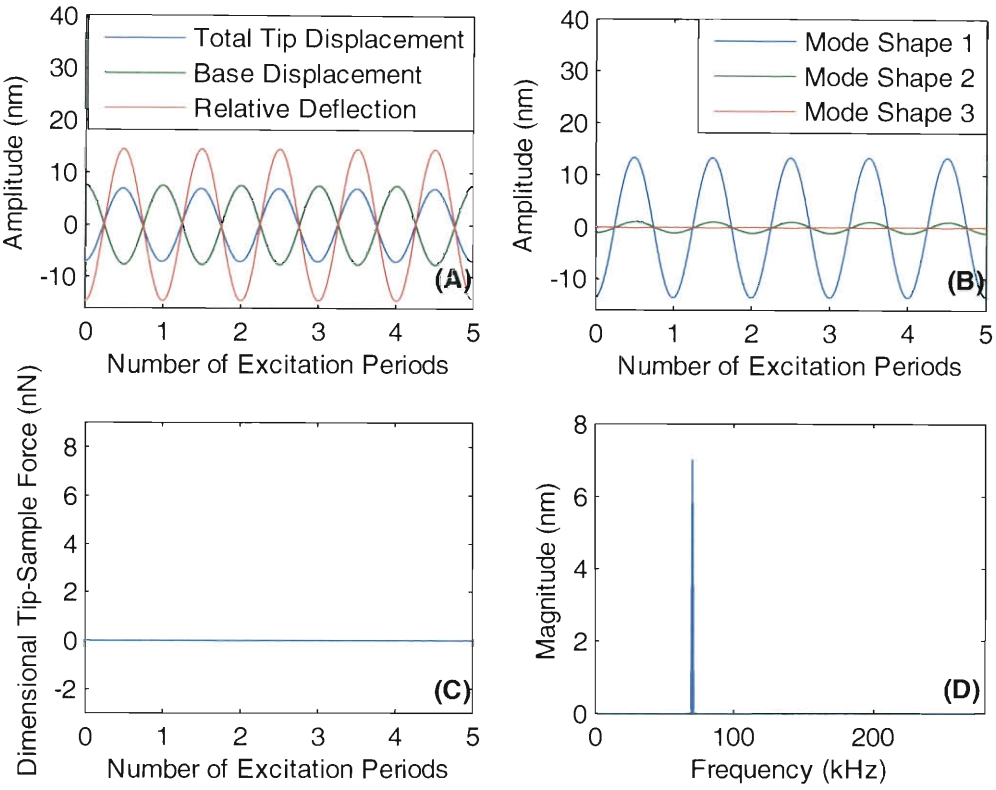

Figure 4-1. Simulation of free oscillation: (A) dimensional total displacement, base displacement and relative deflection, (B) dimensional model response, (C) history of interaction force and (D) spectral information.

the base displacement, the amplitude of total displacement is smaller than the amplitude of the relative deflection.

Then the distance between the rest position of the probe and the sample, *i.e.*, the nominal separation distance $\hat{\delta}$, is decreased incrementally with a step length of $0.1\,nm$. The steady-state responses at every step are recorded for analysis. As the distance is decreased, the probe can experience the tip-sample interaction during its oscillation. The responses at $\hat{\delta} = 7\,nm$ are shown in Figure 4-2.

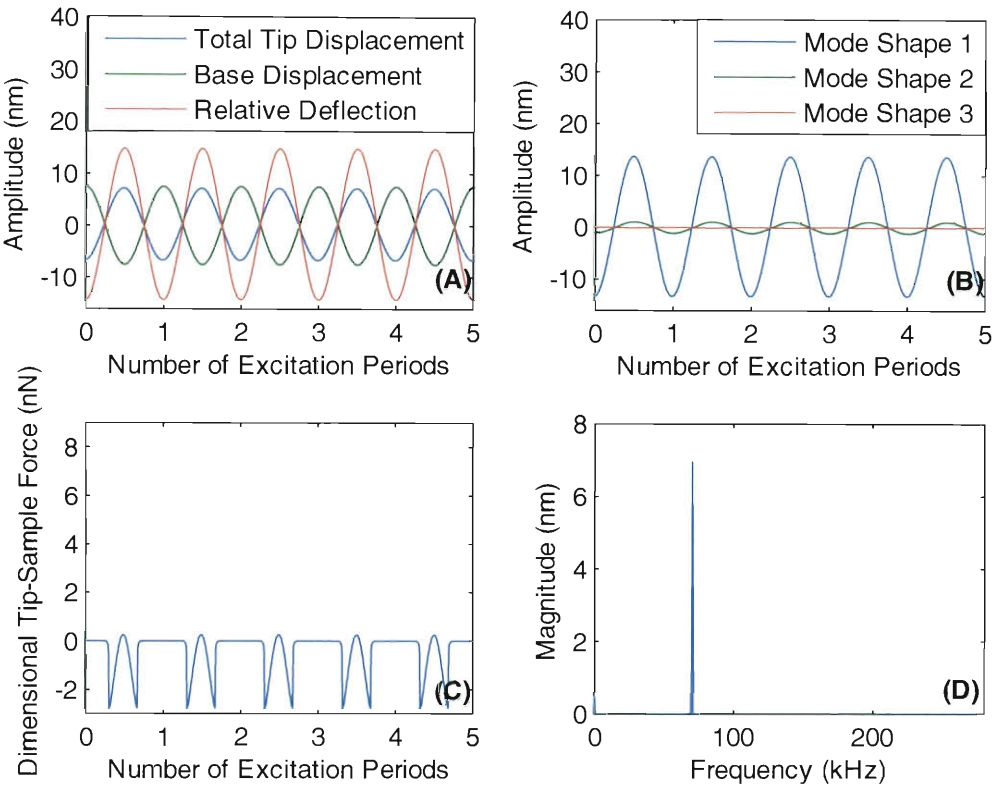

Figure 4-2. Simulation of responses at $\hat{\delta}$=7 nm: (A) dimensional total displacement, base displacement and relative deflection, (B) dimensional model response, (C) history of interaction force and (D) spectral information.

The frequency of the response is still the same as the frequency of the excitation. The tip-sample force curve shows that the tip experiences all three regions of the interaction. The maximum repulsive force is still very small.

As $\hat{\delta}$ continues to decrease, the interaction force level continues to increase. After the repulsive interaction forces have increased sufficiently, a period-two motion is observed. The responses where $\hat{\delta} = 2\ nm$ are shown in Figure 4-3.

In this figure, there are two significant peaks in the spectrum at non-zero frequencies, and the magnitude of the sub-harmonic peak is 1.48 nm. This provides the means to identify

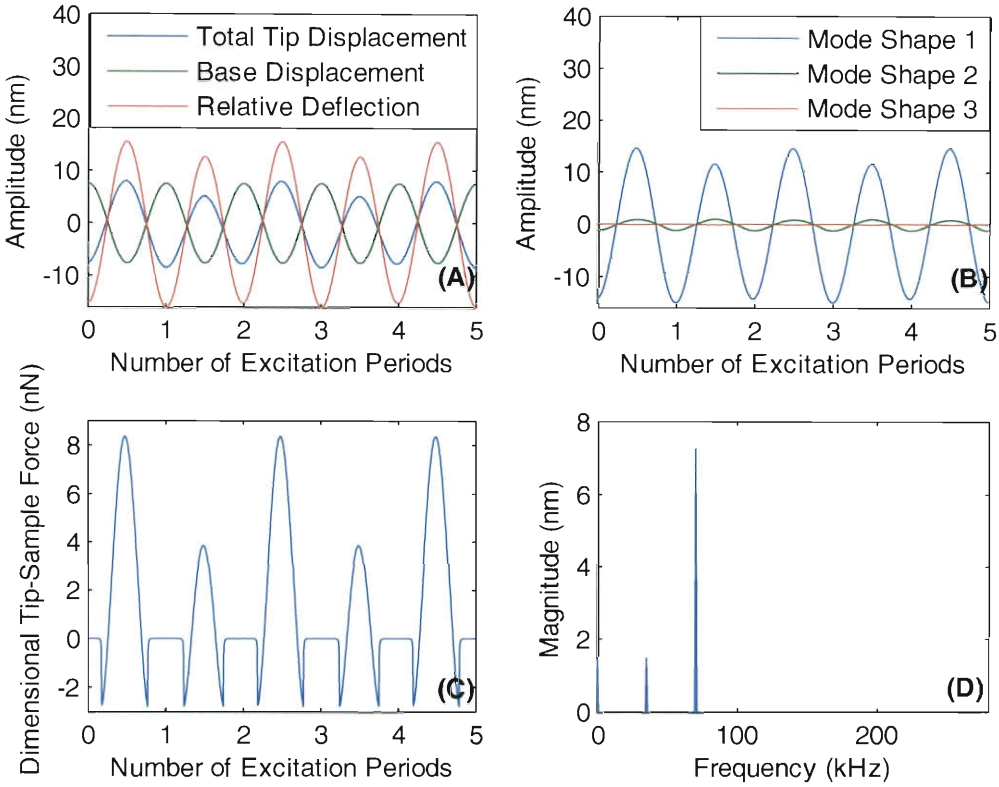

Figure 4-3. Simulation of responses at $\hat{\delta}$=2 nm: (A) dimensional total displacement, base displacement and relative deflection, (B) dimensional model response, (C) history of interaction force and (D) spectral information.

the period-doubling behavior experimentally by monitoring this sub-harmonic frequency component. The maximum repulsive force in Figure 4-3 (C) is 8.36 nN.

As the nominal separation distance continues decreasing, the sub-harmonic component grows and the total response deviates more from the period-one motion. The time series plots and phase portraits corresponding to four different values of the nominal separation distances are illustrated in Figure 4-4. The comparison between the phase portraits of experimental data and simulated data is illustrated in Figure 4-5.

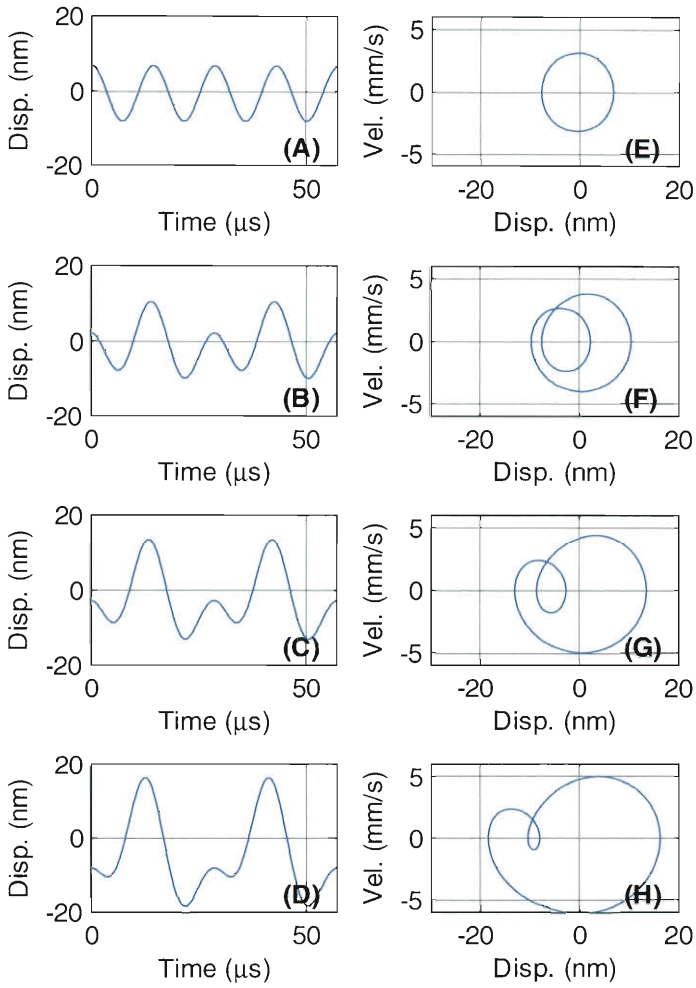

Figure 4-4. Time series plots (A) - (D) and corresponding phase portrait plots (E) - (H) depicting simulated response transition for AFM cantilever probe.

The responses are obtained for the nominal separation distance values of 2.6 nm, 1.5 nm, -0.1 nm, and -2.7 nm. The experimental results and the simulation results in Figure 4-5 are qualitatively similar. The model is verified to be capable of reproducing and studying the bifurcation phenomenon. At the same time, two discrepancies exist. One of them is the change in the mean value of the response. In the experimental results the mean value

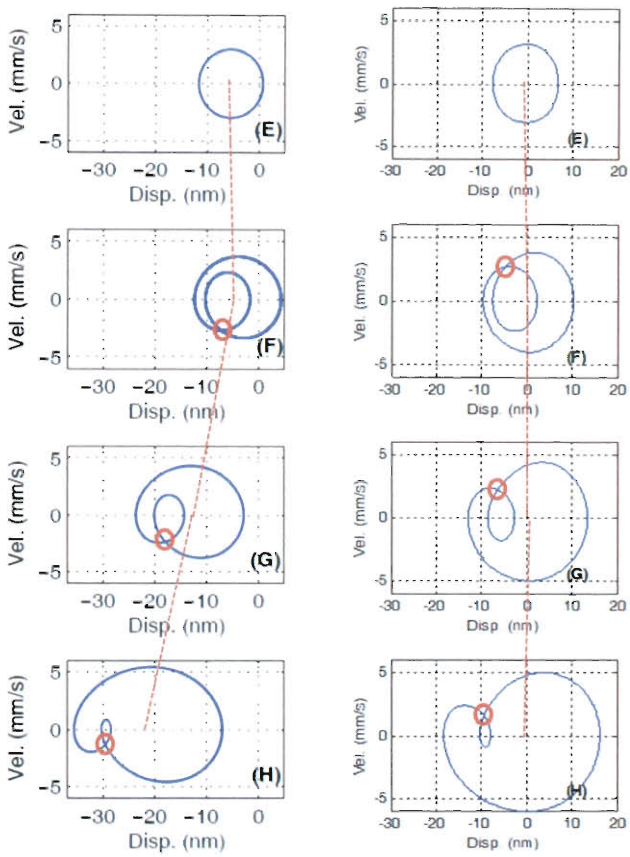

Figure 4-5. The comparison between (left) experimental and (right) simulated data.

moves to more negative values as the nominal separation distance between the probe tip and the sample decreases. The change is not as obvious in the simulation results as in the experimental results. The difference is believed to be caused by potentially larger repulsive force values in the experiment. Since the actual compression is not available in the experiment, the accurate force levels are not possible to be recreated.

The second difference is the orientation of the phase portraits. In the experiment results, the crossing part of the curve is in the lower-left part of the plot. In the simulation results, the crossing part is in the upper-left part of the plot. This implies that the phase differences between the sub-harmonic response and the other significant component are

different in the experimental results and simulation results. This is believed to be caused by the presence of non-conservative tip-sample interactions in the experiment which were not represented in the model. This additional energy dissipation mechanism is believed to significantly affect the phase of the sub-harmonic response and subsequently, the effective orientation of the phase portrait plots.

4.2 The Bifurcation Diagram

This is a bifurcation process and can be visualized more clearly in the bifurcation diagram. In this nonautonomous system, the period of base excitation is used to prepare Poincaré sections. Namely, the value of the deflection is captured when $t - t_0 = 0 \pmod{T}$, in which t_0 is set to correspond to a local maximum total displacement with zero relative velocity. The sampled values are $w_0, w_1, w_2 \dots w_m$, where $m + 1$ is the number of sampled values. Due to the periodicity of the excitation, if $w_0 \approx w_1$, all of the captured values are the same. If $w_0 \approx w_2$ and $w_1 \neq w_0$, the response of which the Poincaré section is collected has a period of two. For each separation distance and steady-state response, a Poincaré section is collected. By plotting this data versus the separation distances, the bifurcation diagram is produced. It is illustrated in Figure 4-6.

Where $\hat{\delta}$ is larger than 2.1 nm, the Poincaré section has only one point corresponding the local maximum value of the total displacement of the period-one motion. The value decreases slowly as $\hat{\delta}$ decreases. After the sub-harmonic component appears, the Poincaré section has two points, indicating the period-two motion. The value of one of them increases as $\hat{\delta}$ decreases, and the value of the other one decreases. The bifurcation point is at around 2.1 nm, which is defined as the critical separation distance. The four

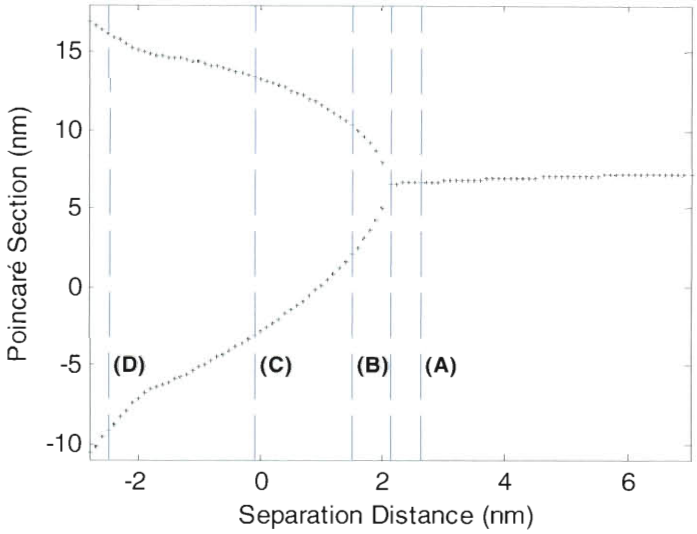

Figure 4-6. Bifurcation diagram constructed from Poincaré sections of the system's response for $\widehat{E^*} = 0.08518\ GPa$. The dashed vertical lines and labels identify the Poincaré sections that correspond to the data presented in the previous plots.

dashed vertical lines and labels correspond to four different separation distance values of the response data presented in Figure 4-4.

For material with different effective modulus, the bifurcation position changes. Several effective modulus values around $0.08518\ GPa$ are used in the simulation and multiple diagrams are produced. The results are presented in Figure 4-7.

The critical separation distance at the bifurcation point is the most significant characteristic of the bifurcation diagram which changes for interaction conditions with different values of the effective modulus. This is related to the interaction level required for the bifurcation to occur. The critical separation distance is lower for smaller effective modulus. This means, using the same probe, more compressions are needed to generate the sub-harmonic component for softer samples. The relation between the critical separation distance and the effective modulus is illustrated in Figure 4-8.

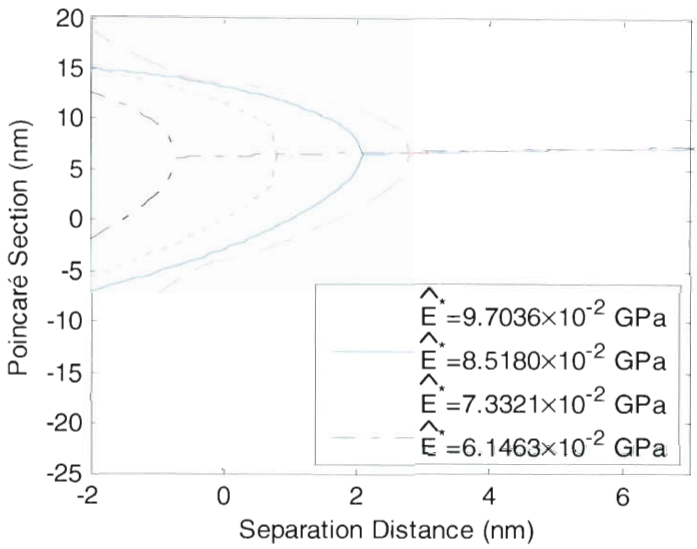

Figure 4-7. Comparison of the bifurcation diagrams constructed from the system's response for a range of different values of $\widehat{E^*}$

.

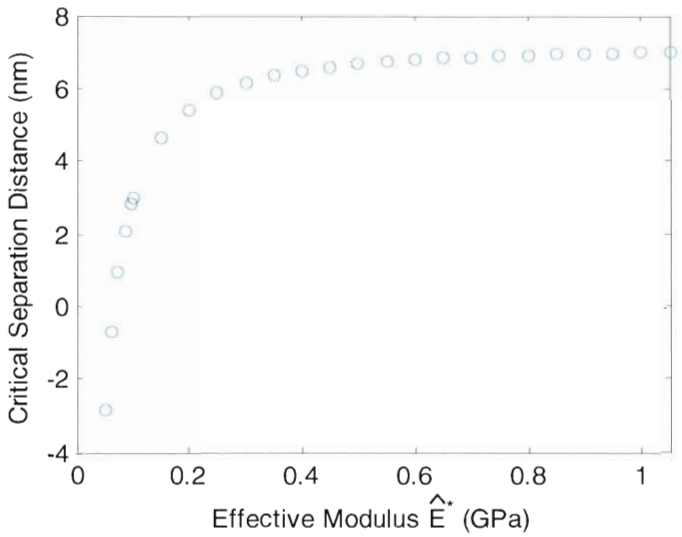

Figure 4-8. Separation distance of period-doubling bifurcation versus the effective modulus

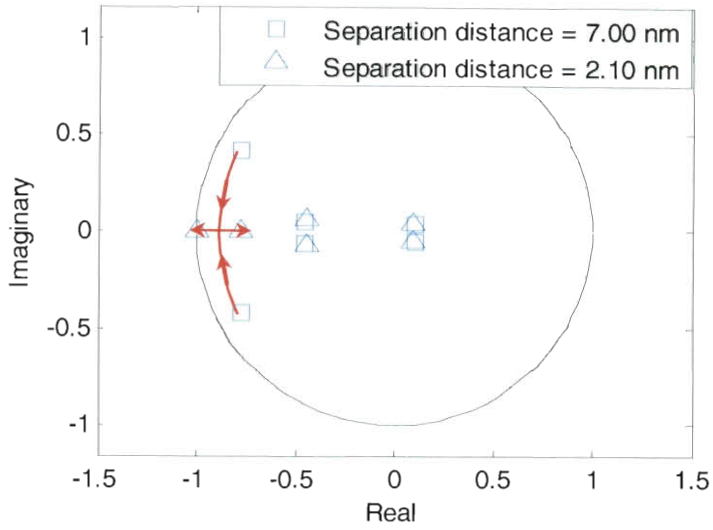

Figure 4-9. Paths of Floquet multipliers before bifurcation as separation distance decreases for $\widehat{E^*} = 0.08518\ GPa$.

The curve in Figure 4-8 is referred to as the nominal case in this thesis, as some other curves are produced and discussed in the parametric study. This behavior is explored as a new source of contrast for mapping the effective modulus of the sample. A method is developed to utilize the critical separation distance of the bifurcation point in order to calculate the effective modulus.

4.3 Floquet Analysis

In order to verify the type of the bifurcation, Floquet multipliers are calculated at each step in the approaching process before the bifurcation. The trends are illustrated in Figure 4-9.

Since three modes are used in the simulation, there are six Floquet multipliers. As shown in the figure, the positions of four of them do not change significantly. The other pairs of Floquet multipliers first approach the real axis, then move away from each other along the real axis. One multiplier is moving to leave the unit circle at -1 before the bifurcation

occurs. According to Floquet theory, this behavior confirms that the bifurcation is a period-doubling bifurcation.

Chapter 5 Parametric Study and the Robustness of the Relations

In the previous chapter, a strong relationship is observed between the critical separation distance and the effective modulus of the tip-sample interaction. However, the influence of other properties of the system on this value must also be investigated. These properties are represented by the excitation amplitude, the environmental damping level, the stiffness of the cantilever and the interaction force model. The excitation amplitude corresponds to the magnitude of the base excitation term. The quality factor characterizes the damping of the operation environment. The cantilever stiffness is determined for a number of commercially available cantilevers. Most interaction force models are only good for certain circumstances and uncertainty surely exists in real measurement. Parametric study is performed in order to investigate the influence of these conditions on probe response behavior. The goal of this study is to determine that if the period-doubling bifurcations occur for a larger range of parameter values and to determine how the critical separation distance is affected. Some of the work in this part is done in dimensionless forms.

5.1 Varying the Excitation Amplitude

The free oscillation amplitude in AFM changes in different modes and for different purposes. A typical free oscillation amplitude in tapping-model atomic force microscope is between 1 nm and 100 nm (García & Rubén, 2002). The value is controlled by the driving signal to the excitation devices, which usually makes use of piezoelectric material.

The actual value may vary due to different components used in different AFM systems, or the capabilities of the actuator. For traditional topographical measurement, the set-point value is set to be smaller than the free oscillation value (50%~95%) to ensure successful intermittent contact. Then the controller adjusts the vertical position of the cantilever base or the sample to maintain the oscillation amplitude at the set-point value during the scan. Since the principle is to maintain the same level of interaction, a perfect controller will make the same amount of adjustment for different levels of excitation amplitude. The measurement value is calculated from the adjustment. Thus it can be insensitive to the changes in excitation amplitudes. For a proposed sample modulus measurement, the quantitative results can be calculated from the ratio between the dimensional critical separation distance and the free oscillation amplitude. If the ratio is insensitive to variations in the excitation amplitude, the calibration work can be reduced. This ratio is identified as the normalized critical separation distance in this thesis. In the nominal case, the free oscillation amplitude is $7\ nm$. Two different excitation levels resulting in free oscillation amplitudes of $5\ nm$ and $10\ nm$ are tested in this part of parametric study. The results are illustrated in Figure 5-1.

These three curves display the same qualitative behavior. Only a small deviation is found for small effective modulus values. The curve for $\widehat{A_0} = 10\ nm$ has the largest deviation, suggesting that responses to larger excitation levels are expected to generate greater deviation. Some work on a one-side constraint impact oscillator also indicated that large changes in the forcing amplitude can change the bifurcation scenario (Ing, Pavlovskaia, Wiercigroch, & Banerjee, 2010). For larger effective modulus values, small deviation exists between the smallest excitation amplitude case and the other cases. For the

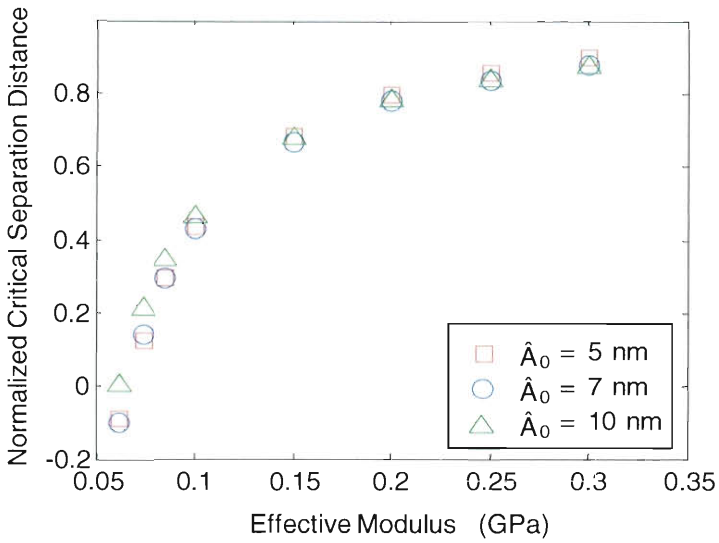

Figure 5-1. Critical separation distance corresponding to period-doubling versus effective elastic modulus for three oscillation amplitudes

conditions studied, the best measurement range is identified as 0.1 GPa to 0.25 GPa. The range can be shifted, however. This will be discussed in the parametric study for varying cantilever stiffness.

5.2 Varying the Quality Factor

The damping in the system can come from the ambient medium, the cantilever itself and the tip-sample interaction. The first two sources are represented by the quality factor Q. Tapping-mode AFM usually operates in an air or liquid environment, the quality factor being $50 - 100$ and about 10, respectively. The experimental work which is mentioned in the beginning of Chapter 3 is conducted in air. However, in the simulation, a high quality factor of 50 will result in the occurrence of the Neimark bifurcations. This behavior is also observed for $Q = 100$. The choice of $Q = 10$ in the simulation is partly

justified since the DMT force model does not include energy dissipation. The lower value of Q is used to compensate for the energy dissipation at the tip-sample interaction between the silicon tip and silicone rubber sample.

5.3 Varying the Cantilever Stiffness

In the tapping mode AFM a standard practice is to select a cantilever based upon the stiffness of the sample. This idea is applicable in this work. Also, different bifurcation behavior is predicted for a much larger ratio of material effective stiffness to the cantilever stiffness (Dick, et al., 2009). Thus it is important to investigate how the cantilever stiffness affects the bifurcation position and within what range the response behavior includes a period-doubling bifurcation.

Three other cantilevers from Bruker Corporation (HMXS-10, DDESP-FM-10 and HMX-10) (Bruker AFM Probes, 2010) are tested. The force constants for them are $1\ N/m$,

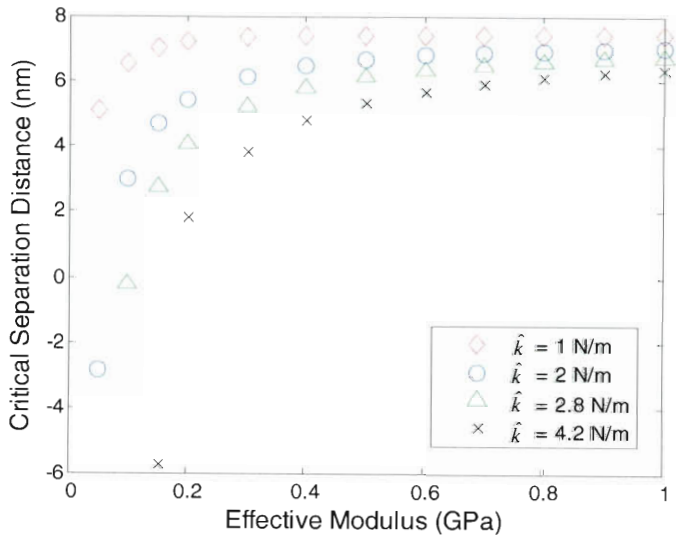

Figure 5-2. Bifurcation diagrams for varying cantilever stiffness

2.8 N/m and 4 N/m, respectively. The results of the simulations are plotted in Figure 5-2. The bifurcations have qualitatively similar characteristic for all four cantilevers. For stiffer cantilever, larger compression is needed for the bifurcation to occur. Since the best range is the middle of the curve where the compression is small and the slope is moderate, stiffer cantilever works better for stiffer materials. Similarly, softer cantilever works better for softer materials.

5.4 Varying the Interaction Model

DMT interaction model is used in this work. However, it is best for stiff material with little adhesion force. The best force model for a particular material is usually unknown and is one property to be measured. In order to study the influence of the form of the model on the bifurcation behavior, the empirical model is also used. The values of the parameters for the empirical model are calculated in the manner presented in Chapter 3. The comparison of the two interaction force models are illustrated in Figure 5-3. The different hardening behavior in the repulsive region should be noted.

The critical separation distance versus the effective modulus curves are illustrated in Figure 5-4. The qualitative trends of the data sets are similar. But the compression for materials with lower effective modulus is considerably larger with the DMT model. This is due to the different hardening behavior. This suggests that the application should be limited in small compression region, and some knowledge of the appropriate interaction force model is desired before the measurement.

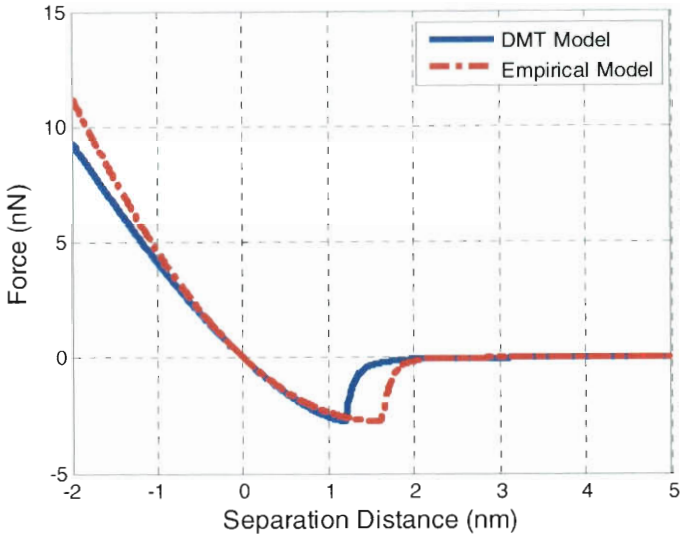

Figure 5-3. Comparison of different interaction force models

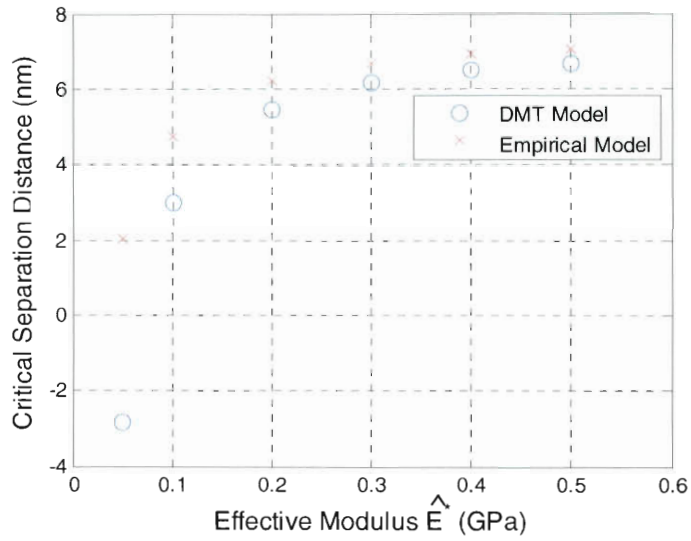

Figure 5-4. Bifurcation diagrams for varying interaction model

Chapter 6 Fast Scan Scheme

Based on the relationship between the critical separation distance and the effective modulus, a scanning scheme is proposed to measure the localized effective modulus with nano-scale resolution. The method is described in this part and some simulated results are presented. The performance of the controller is discussed as well. A step by step description of the proposed implementation of the scan scheme is presented at the end of the chapter.

6.1 Control Algorithm

The control algorithm focuses on keeping the response at the early stage of the period-doubling bifurcation. This is characterized by a small amplitude value of the sub-harmonic component of the response, the frequency of which is one-half of the excitation frequency. This quantity can be measured experimentally by using a lock-in amplifier or with a fast Fourier transform technique. A PID or PI controller is usually used in the tapping mode AFM. In this work, the form of the controller from another work in the tapping mode AFM is used (Solares & Chawla, 2008). During the preparation process before the scan process, the sample is moved towards the excited probe to enable intermittent contact. The nominal separation distance is further reduced to enable the period-doubling bifurcation with the sub-harmonic amplitude equal to a selected set point value A_{Sp}. During the scan process, the control algorithm adjusts the nominal separation distance between the tip and the sample surface, *i.e.* the distance between the rest position of the cantilever base and the sample surface, in order to maintain the sub-harmonic

amplitude at the set-point value. In the simulation the control command is assumed to be calculated and applied at discrete time moments, the separation of which is twice the period of excitation. The algorithm is defined by Equation (6.1) through Equation (6.3).

$$\hat{\epsilon}(n) = K_P\left[\hat{A}_{1/2}\,(n) - \hat{A}_{SP}\right] \tag{6.1}$$

$$\hat{\rho}(n) = K_I \sum_{\mathrm{i}=1}^{\mathrm{N}} \left[\widehat{\mathrm{A}}_{1/2}(\mathrm{n}-\mathrm{i}) - \widehat{\mathrm{A}}_{\mathrm{SP}}\right] \tag{6.2}$$

$$\hat{\delta}(n) = \hat{\delta}(n-1) + \hat{\epsilon}(n) + \hat{\rho}(n) \tag{6.3}$$

In these equations, $\hat{A}_{1/2}$ is the sub-harmonic amplitude, $\hat{\delta}$ is the nominal separation distance between the probe and the sample surface (very close to the critical separation distance for the bifurcation in this case), and n is the index of the discrete time moments. The adjustment contains two parts $\hat{\epsilon}(n)$ and $\hat{\rho}(n)$.The term $\hat{\epsilon}(n)$ is proportional to the error between the current sub-harmonic amplitude and the set-point value. The term $\hat{\rho}(n)$ is a function of the summation of the past N errors. In this study, $\hat{A}_{sp}$ is set to $1\,nm$, which causes a maximum repulsive interaction force of less than $8.36\,nN$ for $\widehat{E^*} = 0.08518\,GPa$, according to Figure 4-3. The parameter N is set to 10. The gains K_P and K_I are tuned for better performance in 1-D scan, which is described later. Their values are set to 0.005 and 0.0001, respectively.

The middle part of the curve in Figure 4-8 is selected as the best measurement range of the cantilever in the test. The curve can be well fitted into an exponential relation. For simplicity, a linear approximation for five points with effective modulus from $0.06\,GPa$ to $0.1\,GPa$ is used. The curve fitting result is Equation (6.4) .

$$\widehat{E^*} = 1.56 \times 10^7 \hat{\delta_c} + 0.0529 \tag{6.4}$$

In this equation, $\widehat{\delta_c}$ is the dimensional critical separation distance in m and $\widehat{E^*}$ is the dimensional effective modulus of the sample in GPa. It should be noted that in the practice, the normalized critical separation distance, which is dimensionless and defined by $\widehat{\delta_c}/\hat{A}_0$, can be used instead of $\hat{\delta}_c$ in Equation (6.4).

6.2 1-D Scan

In order to test the effectiveness of the control algorithm, a number of sample conditions are tested. They are atomic flat with varying effective modulus values. The condition of being atomic flat is used here to simplify the calculation and illustration of the results. In this case, the nominal separation distances during the scan are close to the critical separation distances. If the sample is not flat, the topography should be scanned before, and the critical separation distance is given by subtracting the height of the sample from the nominal separation distance.

The size of the sample is $10\,nm$ and the scan speed is $100\,nm/s$. Three types of variation of the effective modulus are selected to both account for common real variation and testing of the control algorithm. The varying range in all three cases is from $0.8519\ GPa$ to $1\ GPa$. The results are illustrated in Figure 6-1.

The identified value oscillates around the true value and the deviations are small. The sub-harmonic amplitude is also well controlled. A steady-state error exists in these plots, particularly in Figure 6-1 (C). In order to explain this, the relationship between the sub-harmonic amplitude and the nominal separation distance is investigated. This relationship is illustrated in Figure 6-2. The small sub-harmonic amplitude is necessary for the controller and at the critical separation distance the sub-harmonic amplitude

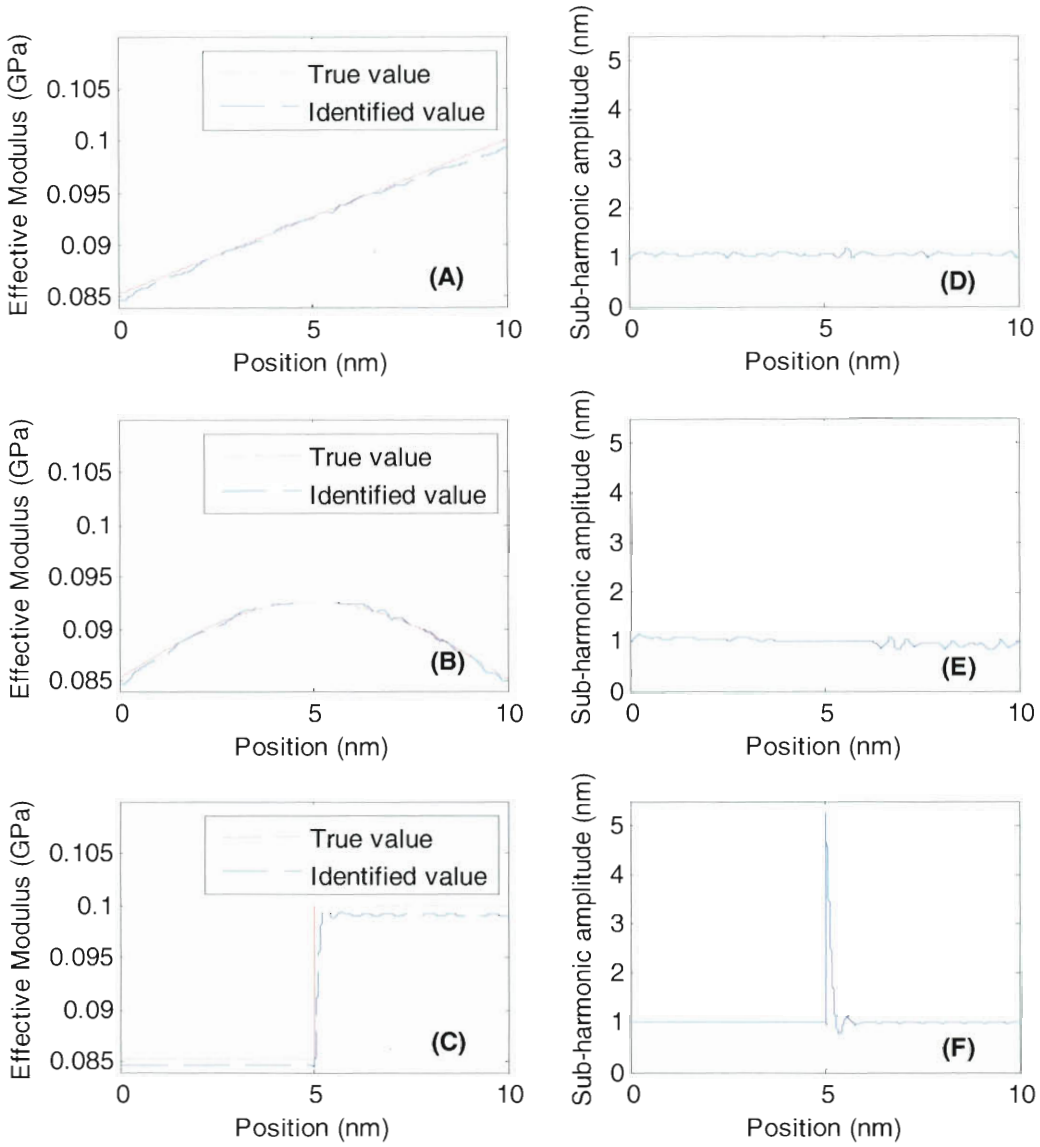

Figure 6-1. The identified effective modulus values (A) - (C) and the monitored sub-harmonic amplitudes (D) - (F) of the simulated scan for atomically flat samples with effective modulus values varying linearly, sinusoidally and abruptly.

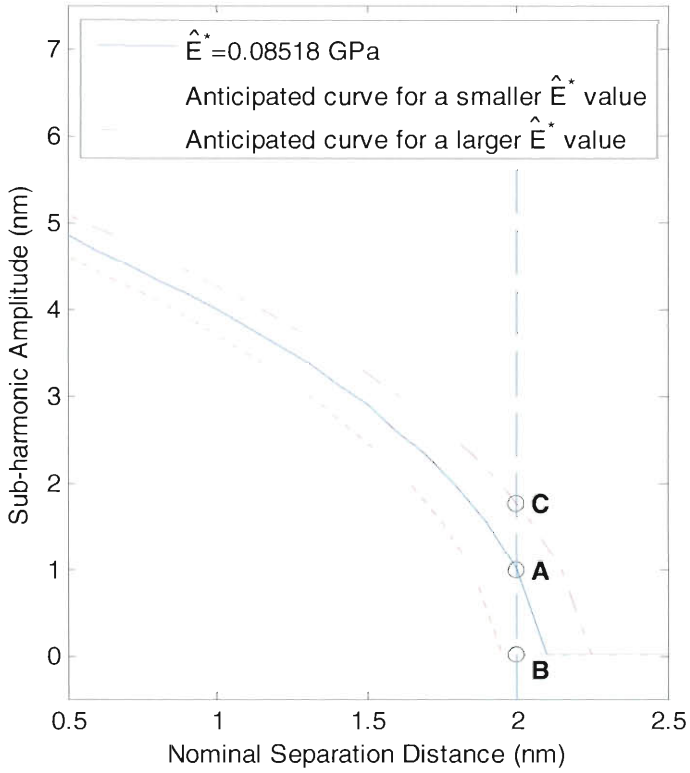

Figure 6-2. The relationship between the sub-harmonic amplitude and the nominal separation distance for $\widehat{E^*} = 0.08518\ GPa$. This relationship is shifted to the left and right side along x axis to provide anticipated curves corresponding to smaller and larger effective modulus values.

should be zero. Thus the controlled separation distance corresponds to the vertical dashed line and is less than the critical separation distance, which is used in Equation (6.4). This error can be reduced by using a smaller set-point value for the sub-harmonic amplitude. The smallest value will depend on the resolution of the data acquisition and analysis module in the AFM, in practice. This error can also be reduced by identifying the relationship between the sub-harmonic amplitude and the separation distance and using it to calculate the effective modulus values.

Two conditions with significant oscillations are noted. One is in Figure 6-1 (E), the oscillation is larger in the second half part of the scan, indicating that the controller performs well to follow the increasing effective modulus, and the performance is not as well when the effective modulus decreases along the scan direction. The two additional dashed curves in Figure 6-2 provide the explanation. The relationship between the sub-harmonic amplitude and the nominal separation distance can be divided into two parts, and the boundary is at the critical separation distance. If the effective modulus of the sample increases, the curve in Figure 6-2 shifts to the right side along the x axis and the monitored sub-harmonic amplitude increases from point A towards point C. These two points are in the same part of the curves. However, if the effective modulus of the sample decreases, the relationship shifts to the left side and the monitored sub-harmonic amplitude decreases from point A towards point B. These two points are in different parts of the curves. In the part where point B is located, the sub-harmonic amplitude does not change as the nominal separation distance changes. The controller is not designed to take this into account. Significant oscillations are also noted at and after the position of discontinuity of the effective modulus, as in Figure 6-1 (C) and (F). The oscillation is believed to be caused by the nonlinearity in the relationship between the sub-harmonic amplitude and the separation distance, and the controller in the tapping mode AFM is designed for a locally linear relationship between the oscillation amplitude and the separation distance. Implementing a nonlinear model for the relationship between the effective modulus and the critical separation distance into the control laws should improve the accuracy of the effective modulus values, which are calculated from the critical separation distances.

6.3 Raster Scan

In this part, the control algorithm is tested in a surface scan. The size of the sample surface is $10\ nm \times 10\ nm$. The sample stage is driven to move in the $x - y$ plan, causing a relative movement of the probe tip with respect to the sample surface. The probe scans back and forth along x axis, and proceeds along y axis when it reaches the edges of the scan area. The scan path is illustrated in Figure 6-3.

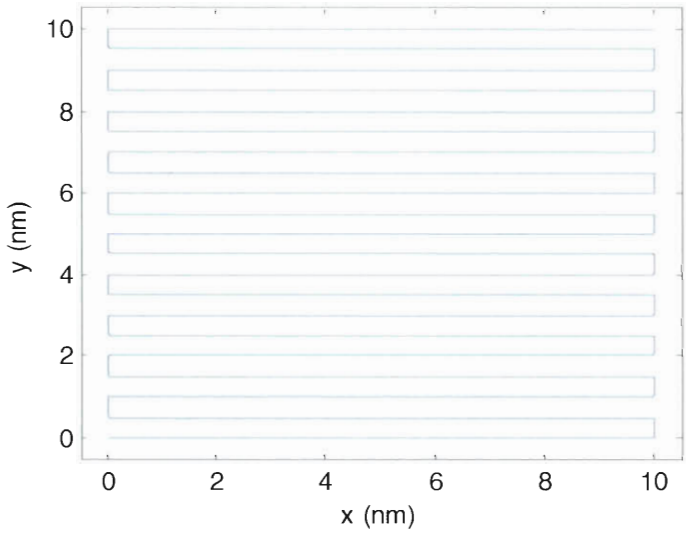

Figure 6-3. The illustration of the relative movement of the probe tip with respect to the sample in the raster scan

Two samples with atomic flat surfaces are simulated. The effective modulus of the first sample varies harmonically along the x axis, and stays constant along the y axis. The distribution is given by Equation (6.5).

$$\widehat{E^*}(x,y) = 0.08518 + 0.01 \times \left(1 + \sin(5\frac{x}{10}\pi)\right) \tag{6.5}$$

In this equation, x and y are the dimensional coordinates in nm and $\widehat{E^*}$ is the dimensional effective modulus of the sample in GPa.

This distribution favors the proposed raster scan, since the resolution along the x axis is much higher than the resolution along the y axis, and for this distribution, only the information along the x axis is important. The results are illustrated in Figure 6-4 as a 3D surface plot and in Figure 6-5 as contour plots. The contour plot of the identified values is produced by the interpolation of the curve in the 3D surface plot.

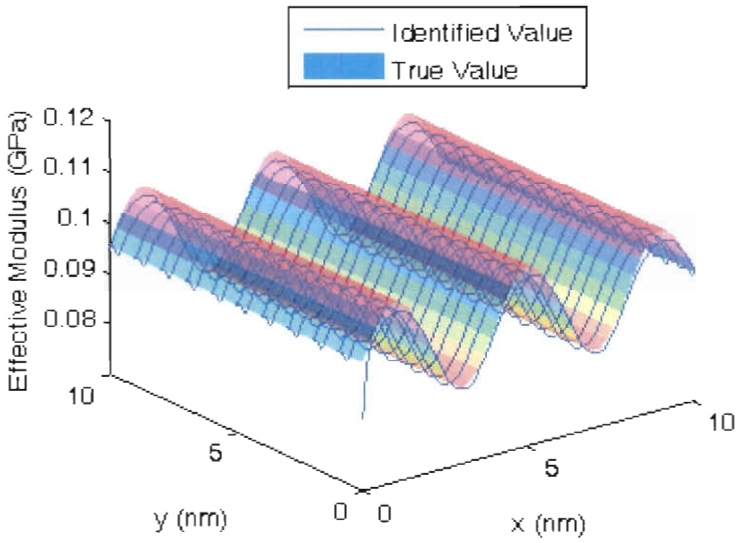

Figure 6-4. The identified values and true values of the effective modulus of sample one, represented in 3D surface plot.

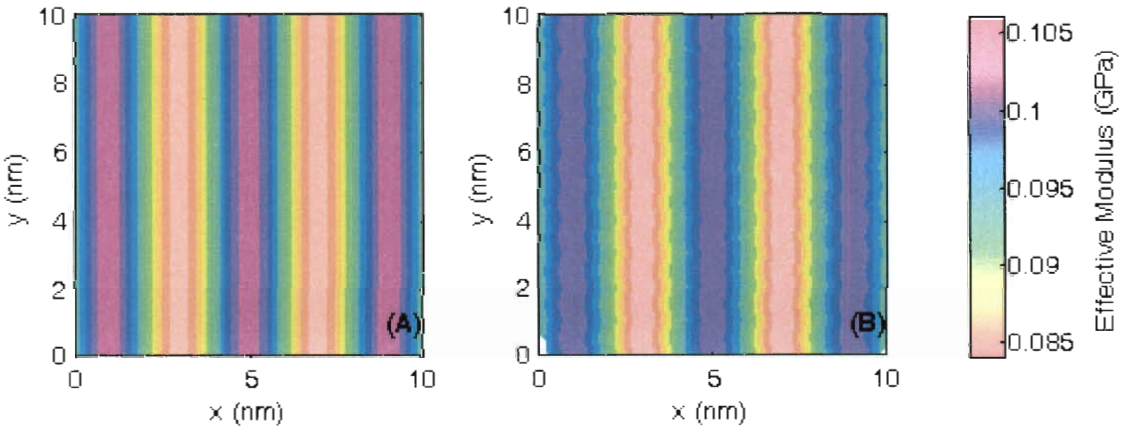

Figure 6-5. The (a) true values and (b) identified values of the effective modulus of sample one, represented in contour plots.

The identified values agree well with the true distribution. Two discrepancies are observed. One is that the identified values are lower than the true value, the reason of which is that the nonzero sub-harmonic amplitude corresponds to a smaller separation distance than the critical separation distance. The second one is the "saw-tooth" along the edge of the stripes in the contour plot. This is caused by the two opposite scan directions along the x axis and the delay in the response of the control algorithm to the variances of sample properties. It is noted that the delay is more significant than the delay in Figure 6-1 (B). This is because the rate of variance of the effective modulus here is faster than the one in the 1-D scan.

The effective modulus of the second sample varies along both the x axis and the y axis. The distribution is given by Equation (6.6).

$$\widehat{E^*}(x,y) = 0.08518 + 0.01 \sin\left(\frac{x}{10}\pi\right) \sin\left(\frac{y}{10}\pi\right) \tag{6.6}$$

In this equation, x and y are the dimensional coordinates in nm and $\widehat{E^*}$ is the dimensional effective modulus of the sample in GPa.

The results are illustrated in Figure 6-6 as the 3D surface plot and in Figure 6-7 as contour plots.

The identified values agree with the true distribution, but the agreement is not as good as the previous simulation. The identified values are again lower than the true values. Another discrepancy is that a significant amount of oscillations are generated in the identified value. These oscillations are more significant in the part where the effective modulus is decreasing. This implies that the control algorithm follows increasing effective modulus values better than decreasing effective modulus values. This is

believed to be caused by the nonlinearities in the relationship between the sub-harmonic amplitude and the compression, and the use of a linear control algorithm.

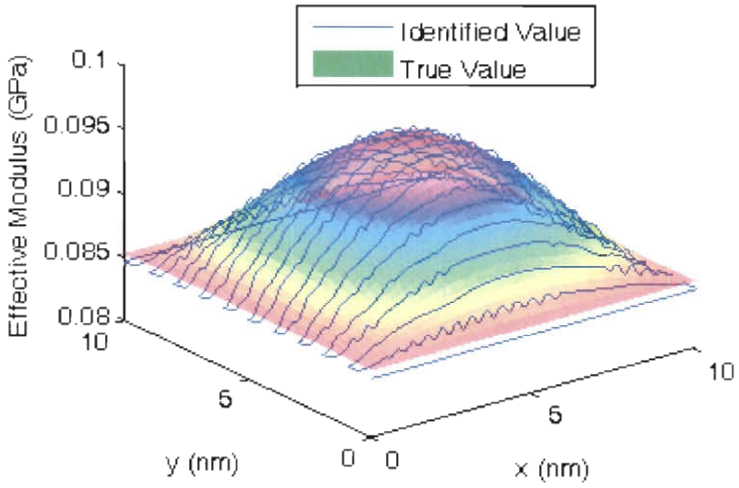

Figure 6-6. The identified values and true values of the effective modulus of sample two, represented in 3D surface plot.

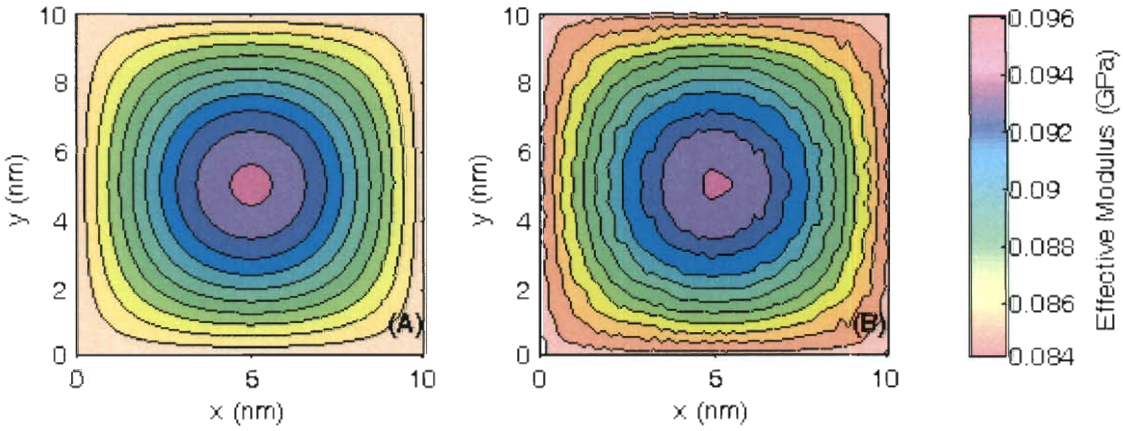

Figure 6-7. The (a) true values and (b) identified values of the effective modulus of sample one, represented in contour plots.

6.4 Summary of the Scan Scheme

As a summary, the proposed scan is to be conducted through these steps:

1) The AFM is operated in tapping-mode and used to measure the topography of the sample. This function is available in tapping-mode AFM equipment already. The determination of the exact location of the effective surface of the sample is being improved for better accuracy by new methods (Dick, et al., 2009).
2) At the starting position of the scan, the separation distance between the tip and the sample is set to a large value to avoid significant interaction. The driving frequency is set to two-and-a-half times the fundamental frequency of the cantilever probe. The level of the excitation is tuned to generate moderate oscillation amplitude.
3) Based on the knowledge of the location of the effective surface of the sample, the nominal separation distance between the rest position of the tip and the sample surface can be determined. The nominal separation distance between the tip and the sample is decreased while the amplitude of the sub-harmonic component at half of the excitation frequency in the response is monitored. This process stops when the amplitude reaches a small set-point value. At this moment, the nominal separation distance corresponds to a value close to the critical separation distance.
4) The tip is moved laterally on the sample surface along pre-defined scan path (*e.g.* ruster scanning path), while the controller is adjusting the nominal separation distance to maintain the sub-harmonic amplitude at the set-point value. The values of the nominal separation distance and the topographical information are used to

calculate the critical separation distance or normalized critical separation distance along the scan path.

5) The relationship between the effective modulus of the sample and the critical separation distance or the critical separation distance is used to calculate the effective modulus of the sample. In the simulation, Equation (6.4) is used as the relationship. However, in the practice, the reconfirmation or calibration of this relationship should be done through the measurement on samples with known values of the effective modulus.

Chapter 7 Concluding Remarks

7.1 Summary

This work is focused on the period-doubling bifurcation in atomic force microscopy. This nonlinear phenomenon has been observed in the constrained oscillation systems before, but its potential application is not previously identified and studied. In this work, one significant characteristic of the period-doubling bifurcation, *i.e.* the critical separation distance, is related to the effective modulus of the tip-sample interaction in tapping mode AFM. The relationship can be combined with a scan scheme to form a fast mapping method for localized material properties. This method does not require special fabrications and can avoid strong destructive interaction forces.

The multi-mode approximation and the Galerkin method are used in order to prepare a model to simulate the behavior of the AFM probe. The model is capable of capturing the nonlinear behavior in the approaching process. The model can be improved if the energy dissipation can be modeled more accurately, but the identified relationship between the effective modulus and the critical separation distance at the period-doubling bifurcation point is believed to be relevant to AFM dynamics.

Through the parametric study, the qualitative bifurcation behavior is confirmed to be robust in a range of parameter values. The quantitative differences can be reduced by choosing ideal operating conditions. In this work the preferred environment requires high damping levels either within the operating environment or at the tip-sample interface.

Simple designs of the controller and scan scheme verifies that the study of the period-doubling bifurcation is promising in developing a new fast mapping method for the

effective modulus. The controller in this work is linear, and it is believed that the use of a nonlinear controller will improve the performance of the material characterization scheme.

7.2 Future Work

In order to improve performance, an improved model of the interaction force, more parametric studies, and the development of a nonlinear control can be explored. A bifurcation analysis, which uses analytical or semi-analytical method to reproduce and study the bifurcation, is desired as well in order to understand the causes of this bifurcation and to improve the efficiency of the implementation and accuracy of the control algorithm. Finally, the experimental verification should be done.

Reference

Bruker AFM Probes. (2010). Retrieved 11 14, 2010, from http://www.brukerafmprobes.com

Asylum Research. (n.d.). Retrieved from Asylum Research Web site: http://www.asylumresearch.com/Probe/AC240TM,Olympus

Binning, G., Quate, C. F., & Gerber, C. (1986, Mar). Atomic Force Microscope. *Phys. Rev. Lett., 56*(9), 930-933.

Dankowicz, H. (2006). Nonlinear dynamics as an essential tool for non-destructive characterization of soft nanostructures using tapping-mode atomic force microscopy. *Philosophical Transactions of the Royal Society A, 364*, 3505-3520.

Derjaguin, B. V., Muller, V. M., & Toporov, Y. P. (1975). Effect of contact deformations on the adhesion of particles. *Journal of Colloid and Interface Science, 53*(2), 314-326.

Dick, A. J., & Huang, W. (2010). Period-doubling bifurcations in atomic force microscopy. *Proceedings of the ASME International Design Engineering Technical Conferences and Computers and Information in Engineering Conference 2009, DETC2009*, *6*, pp. 553-562. San Diego, CA, August 30 - September 2, 2009.

Dick, A. J., Balachandran, B., Yabuno, H., Numatsu, M., Hayashi, K., Kuroda, M., et al. (2009). Utilizing nonlinear phenomena to locate grazing in the constrained motion of a cantilever beam. *Nonlinear Dynamics, 57*(3), 335-349.

Doedel, E. J. (1981). AUTO: a program for the automatic bifurcation analysis of autonomous systems. *Congressus Numerantium, 30*, 265-284.

García, R., & Rubén, P. (2002). Dynamic atomic force microscopy methods. *Surface Science Reports, 47*, 197-301.

Giessibl, F. J. (2001). A direct method to calculate tip-sample forces from frequency shifts in frequency-modulation atomic force microscopy. *Applied Physics Letters, 78*(1), 123-125.

Huang, W., & Dick, A. J. (2010). Localized material properties through nonlinear dynamics based atomic force microscopy. Presented in *2010 ASME International Design Engineering Technical Conferences and Computers and Information in Engineering Conference.* Montreal, Quebec, Canada, August 15 - 18, 2010.

Hurley, D. C., Kopycinska-Müller, M., Kos, A. B., & Geiss, R. H. (2005). Nanoscale elastic-property measurements and mapping using atomic force acoustic microscopy methods. *Measurement Science and Technology, 16*, 2167-2172.

Ing, J., Pavlovskaia, E., Wiercigroch, M., & Banerjee, S. (2010). Bifurcation analysis of an impact oscillator with a one-sided elastic constraint near grazing. *Physica D, 239*, 312-321.

Johnson, K. L., Kendall, K., & Roberts, A. D. (1971). Surface energy and the contact of elastic solids. *Proceedings of the Royal Society of London. Series A, Mathematical and Physical Sciences, 324*, 301-313.

Lee, S. I., Howell, S. W., & Raman, A. R. (2003). Nonlinear dynamic perspectives on dynamic force microscopy. *Ultramicroscopy, 97*(1-4), 185-198.

Legleiter, J., Park, M., Cusick, B., & Kowalewski, T. (2006). Scanning probe acceleration microscopy (SPAM) in fluids: Mapping mechanical properties of surfaces at the nanoscale. *PNAS, 103*(13), 4813-4818.

Maugis, D. (1992). Adhesion of spheres: The JKR-DMT transition using a dugdale model. *Journal of Colloid and Interface Science, 150*(1), 243-269.

Nayfeh, A. H., & Balachandran, B. (1995). *Applied Nonlinear Dynamics: analytical, computational, and experimental methods.* Wiley.

Sahin, O., Magonov, S., Su, C., Quate, C. F., & Solgaard, O. (2007). An atomic force microscope tip designed to measure time-varying nanomechanical forces. *Nature nanotechnology, 2*, 507-514.

Solares, S. D., & Chawla, G. (2008). Dual frequency modulation with two cantilevers in series: a possible means to rapidly acquire tip-sample interaction force curves with dynamic AFM. *Measurement Science and Technology, 19*, 055502 (8pp).

Solares, S. D., & Crone, J. C. (2007). Real-time simulation of isolated biomolecule characterization with frequency and force modulation atomic force microscopy. *Journal of Physical Chemistry C*, 10029-10034 .

Stark, M., Guckenberger, R., Stemmer, A., & Stark, R. W. (2005). Estimating the transfer function of the cantilever in atomic force microscopy: A system identification approach. *Journal of Applied Physics, 98*(11), 114904.

Stark, R. W. (2010). Bistability, higher harmonics, and chaos in AFM. *Materials today, 13*(9), 24-32.